SCALING IN DIRECTIONAL SOLIDIFICATION OF BINARY ALLOYS

SCALING IN DIRECTIONAL SOLIDIFICATION OF BINARY ALLOYS

By

MICHAEL GREENWOOD

B.Sc Physics and Computer Science, Dalhousie University

A Thesis

Submitted to the School of Graduate Studies

in Partial Fulfilment of the Requirements

for the Degree

Master of Applied Science

McMaster University

MASTER OF APPLIED SCIENCE (2004) McMaster University

(Material science) Hamilton, Ontario

TITLE: Scaling in directional solidification of binary alloys

AUTHOR: Michael Greenwood, B.Sc.(Dalhousie University)

SUPERVISOR: Dr. Nikolas Provatas

NUMBER OF PAGES: 101

Abstract

This thesis summarizes work done in the simulation of cellular and dendritic growth in directional solidification of dilute binary alloys using a phase-field model. This model is solved on a dynamic adaptive grid using a linear isoparametric formulation of the finite element method. The spacing of the primary dendritic branches are examined for a wide range of thermal gradients and alloy compositions using a power spectral analysis technique. This spacing is found to undergo a maximum as a function of increasing velocity, in agreement with experimental observations. Our simulations are compared to directional solidification experiments of PVA-ETH, SCN-ACE and SCN-SAL alloys and we demonstrate that the spacing selection is described by a crossover scaling function from the emergence of cellular growth into the dendritic growth regime. This scaling function is dependent upon only dimensionless groupings of the material dependent lengthscales and the process parameters at which the system is cooled. We validate our results by showing that both the simulated materials and published experimental data collapse onto this single universal curve.

ACKNOWLEDGEMENTS

I would like to acknowledge my supervisor Dr. Nikolas Provatas for the all aid he has given me during the course of my thesis and for his neverending support over the last two years. I would also like to thank the members of our group, in particular Jun Fan with whom I spent many a time working on some problem or another, or would lend me a paper I had misplaced. I would like to acknowledge the aid given to me by our Post Doc, Dr. Mikko Haataja for his assistance in the development of this thesis and wish him well with his new position at Princeton University.

This thesis would never have been completed without financial support, therefore I would like to acknowledge the Center for Automotive Materials at McMaster University. I would also like to thank the people at SharcNet, in particular the system administrator Mark Hahn for his quick responses and smooth running of the computer facilities here at McMaster.

I would also like to thank the Materials Science and Engineering department and its staff whom all work very hard to keep things running while we live in our little worlds.

And finally the various factions of my friends and family scattered about this planet.

Contents

List of Figures

Nomenclature

α	Thermal diffusion constant
$\bar{\lambda}_1$	Dimensionless scaled primary wavelength
$\bar{V}$	Dimensionless scaled velocity
β	Interface kinetics coefficient
ΔC	Difference between solidus and liquidus concentrations
ΔG_r	Gibbs Free energy difference for nucleation of radius r
ΔG_v	Gibbs Free energy difference for bulk phase
ϵ_4	anisotropy constant
γ	Interfacial energy
κ	Local curvature
λ	Free parameter proportional to the nucleation energy

λ_1 Primary dendrite spacing

λ_C Onset critical wavelength

λ_{MS} Mullins-Sekerka wavelength

λ_{theory} Theoretical calculation of the onset critical wavelength

μ Chemical potential

ν Stability parameter

ν_o Unit volume

ω_k Amplification rate

ϕ Order Parameter

τ Characteristic time of a simulation

$A(\vec{n})$ Anisotropic function

a_t Anti trapping coefficient

C Solute concentration

C_L Concentration from the liquidus side of the binary phase diagram

C_o Initial alloy concentration

C_o^l The liquidus concentration corresponding to C_o

c_p Specific heat at constant pressure

C_S Concentration from the solidus side of the binary phase diagram

C_{eq} Equilibrium concentration

C_{int} Concentration on the interface

D Generalized solute diffusion coefficient

D_L Solute diffusion coefficient in the liquid phase

d_o Generalized capillary length

d_o^C Chemical capillary length

d_o^T Thermal capillary length

D_S Solute diffusion coefficient in the solid phase

E Finite element error approximation

F Free energy

f_k frequency corresponding to wavenumber k

f_{AB} Bulk free energy

G Thermal Gradient

G_L Gibbs Free energy in the liquid phase

G_S	Gibbs Free energy in the solid phase
K	Solute partition coefficient
k	Wave frequency
k_B	Boltzmann's constant
k_{mean}	Weighted mean average wavenumber
L	Latent heat of fusion
l_D^*	Diffusion length at the onset critical velocity
l_D	Diffusion length
l_T	Thermal Length
l_{TR}	Variable Thermal Length
m_l	Liquidus slope
n_o	Number of atoms
n_r	Number of nucleation sites of radius r
P_k	Power of wavenumber k
R	Gas constant
r	radius of nucleation

T	Temperature
t	Time
T_M	The melting temperature
T_{int}	Temperature on the interface
U	Dimensionless temperature field
V	Velocity
V_C	Planar to unstable critical velocity
W	Interface width
x_N	Normalized tip length
x_{root}	Position of the base of the dendrite
x_{tip}	Tip position of the dendrite
y_N	Normalized dendrite width
y_{max}	Maximum width of a dendrite from its center

Chapter 1

Introduction

It is well known that the microstructure of materials establishes many of their industrially important mechanical properties. In the manufacture of industrially cast alloys some of the most time-consuming and expensive processes are focused on the control and refinement of microstructure. The first, and perhaps most important, step in the formation of the alloy is the solidification process. This process establishes the initial length scales and morphology of the microstructure. The length scales established during soldification set the scaling of microstructure during subsequent thermomechanical processing. Understanding microstructure formation during solidification is therefore an important step in the formation of metal alloys.

This thesis will examine microstructure formation in directionally solidified binary alloys of succinonitrile(SCN) and pivalic acid(PVA). These are both transparent organic alloys(often refered to as "organic analogues of metals") which are amenable to direct in-situ

observation during the solidification process. We quantify dendritic spacing selection for directional solidification as a function of the process parameters as well as the alloy composition.

This thesis has 6 chapters. Chapter 1 will give an overview of solidification. We will begin with a review of the theory of nucleation and grain growth and their importance in the mechical properties of alloys. In this section we will cast the kinetics of solidification in the context of a sharp-interface mathematical model that self-consistently describes the interplay of reaction, diffusion, surface tension and non-equilibrium kinetics during solidification. We will use this model to elucidate the length and time scales that enter into microstructure selection. Chapter 2 will introduce the phase-field method as a more fundamental and efficient method to model solidification and other phase transformation phenomena. Chapter 3 will discuss a new computational method developed for very efficient multi-scale simulation of phase-field(and related) models. Chapter 4 begins with an examination of recent directional solidification experiments, conducted at McMaster university by Dr. Jack Kirkaldy's group. The experiments will form the back drop against which we will validate our modeling results. We report on new directional solidification simulations for material and process parameters similar to those of the above experiments, and propose a new way to examine wavelength selection in directional solidification based on power spectrum analysis. Chapter 5 ties together experiments and simulations by introducing a universal scaling function that has been developed to describe wavelength selection over a wide range of alloys and solidification process parameters. Chapter 6 concludes and

discusses our results.

1.1 Strength and Microstructure

Many different lengths scales are inherent in matter, and each has their own importance in determining the overall properties of materials. The nanoscopic scale deals with atoms and their interactions. In a solid the atoms are bound together, and in the case of a crystal can be arranged into organized lattice structures. But generally this organization is imperfect. Atoms can be missing from their lattice positions or can be sitting between other atoms, both of which cause distortions of the lattice. These imperfections are called vacancies and interstitials, respectively. Other crystal defects exist in the form of dislocations, where an extra crystal plane is inserted in the lattice, causing a dislocation line in the crystal. When a material is deformed, new dislocations are created and the dislocation lines move around. A material's strength is largely due to the interaction of dislocations with each other and with grain boundaries.

In the perfect material the energy of fracture is enormous, as one needs to break every bond between every atom along a plane. Defects allow for the concentration of applied stresses, leading to material deformation at much lower energy, due to dislocation cores moving about. A determining factor of the strength of a material is how easily these cores can move. A dislocation core can look much like in figure 1.1 (left). For the core to move we must slide the extra plane of atoms over by one plane. An applied force overcomes an

energy barrier, bonds are broken and reattached afterwards. Figure 1.1 (middle) and (right) shows the core as it moves along in a process called 'glide'. The energy barrier needed to overcome is directly proportional to the atomic bonds between the atoms, for the core to move it must break a bond. This also reflects the fact that different materials with different atomic bonds will result in different material stiffnesses.

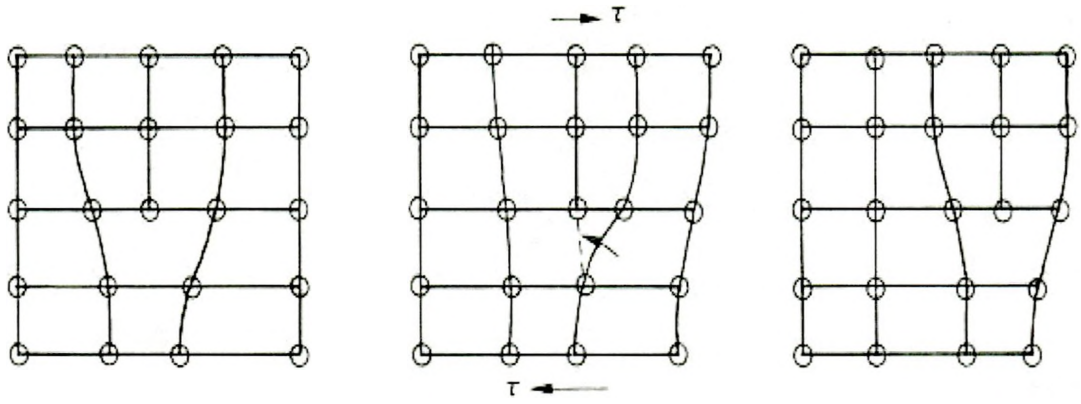

Figure 1.1: *Left: A dislocation in a crystal structure. Middle: Shear force applied causing the atomic planes to shift. Right: Dislocation has moved to the right.[50]*

In most cast materials the motion of dislocations is controlled by structure at the microscale. When a crystal is formed it is made of many impinged crystal grains all with different orientations, as shown in figure 1.2. This grouping of materials is classified as a polycrystal. In any given crystal, or grain, within the polycrystal, there will be dislocations. These dislocations will move about when forces are applied. But when a core attempts to pass from one grain to another, the direction of the core must be changed to correspond with the crystalline orientation of the new grain, see figure 1.3. This results in the necessity

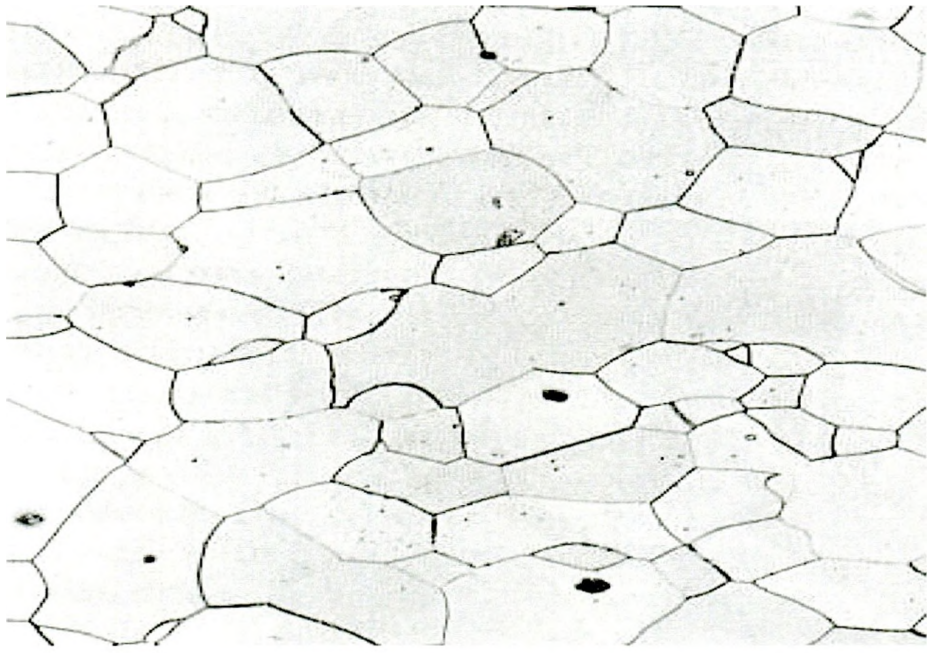

Figure 1.2: *Grain structure.[71]*

of applying more force to move the dislocation.

From this argument one could hypothesize that the more times a dislocation has to change its direction in the course of an applied force, the harder the material is to plastically deform as it requires the extra energy to move the cores around. This would mean that a higher density of crystals with differing orientations would result in a material that would require more energy to plastically deform. While this is only part of what actually goes on, it has been shown that as the size of the grain gets smaller, the strength of the material increases, this is shown in figure 1.4.

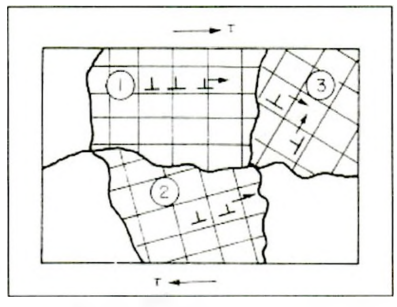

Figure 1.3: *Dislocations move through grains and must change directions if they pass from one grain to another.[50]*

Since the grain size is a factor in how strong a material will be, an important question to ask is: "What sets the length scales of the grains?"

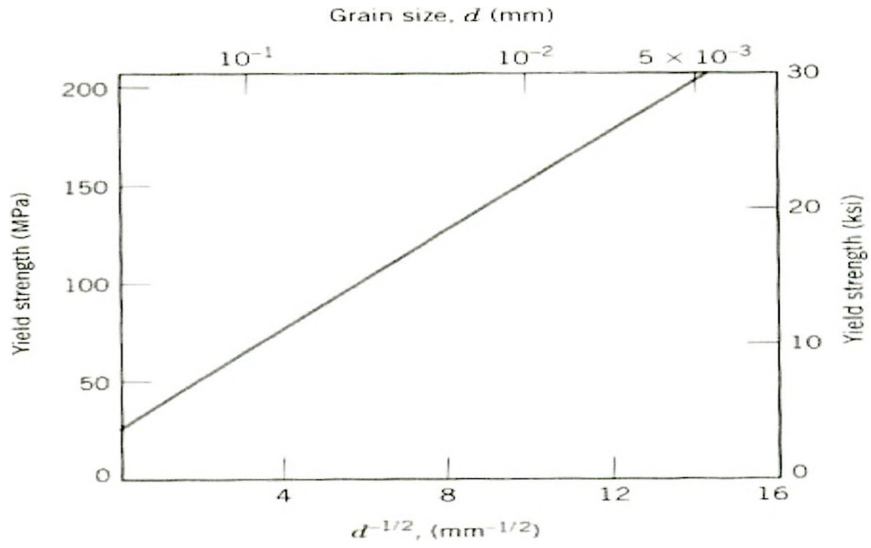

Figure 1.4: *The Hall Petch Relationship.[71]*

1.2 Solidification: Applications

Part of determining how to predict the grain size is first determining how the grains form and how they form is in turn determined by the process in which a material has been cast. The factors which can determine this ultimate outcome vary from the materials used to the cooling process.

Traditionally when a metal is cast into ingots it is first cooled and then after the initial structure has been established, the metal is cold rolled, or themo-mechanically processed to

obtain a desired microstructure. This type of treatment results in an alteration of the initially formed dendritic grains, but is very energy and time consuming. New techniques have been developed that use reduced amounts of cold rolling and thermo-mechanical treatment after casting. This results in a decrease in energy and time in the casting process, and therefore a decrease in the cost. However, such processes leave much of the original as-cast structure intact, making the importance of pattern prediction in solidification a critical step in controlling the overall product quality of such alloys.

One such technique is called strip casting. Strip casting, fig 1.5, involves taking a molten metal, running it through rollers or belts, at a set cooling rate producing sheets of metal that are coiled with minimal cold rolling. Therefore, the original cast structure is prominent in the metal and this structure will influence the properties of the alloy formed.

Another example in which the original cast structure is important is in the formation of turbine blades. Since turbine blades move very quickly in a circular direction, most of the applied force is centripetal, due to the rotation. The casting procedure often used to form these materials is directional solidification. This causes the grains formed to be long and in the direction of the force. But the original cast structure is maintained in the solidified material and prediction of grain sizes is important in obtaining an optimized material.

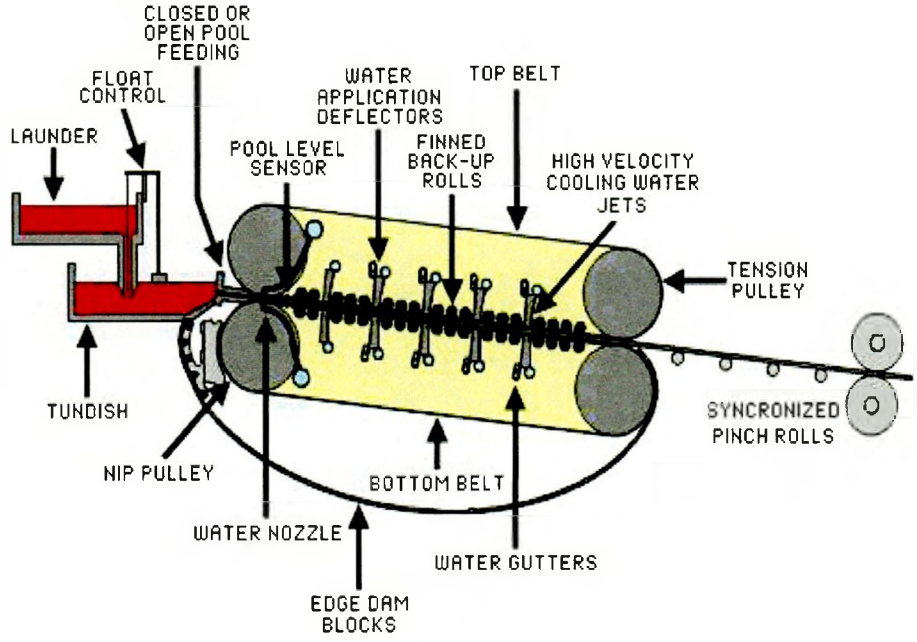

Figure 1.5: *Schematic of a twin belt strip caster.(Image from Hazelett corp. www.hazelett.com)*

1.3 Solidification: Overview

The general theory of solidification will be reviewed, starting with the basics of nucleation followed by solidification in pure materials and binary materials. We will then review previous work on dendritic growth. Directional solidification will then be introduced and some of the work done in this field will be reviewed. The important length scales of solidification are discussed and two theories of controlling the formation of dendritic instabilities will be discussed.

1.3.1 Solidification: Nucleation Theory

Solidification is the process of going from a disordered liquid state into an ordered crystalline state when the temperature is lowered below the melting temperature T_M. The driving force for solidification is governed by the free energy. When the temperature is sufficiently lowered ($T < T_M$) the bulk Gibbs free energy of the solid becomes lower than that of the Gibbs free energy of the liquid. When this occurs the liquid will be driven towards the lower energy state, and solid will form.

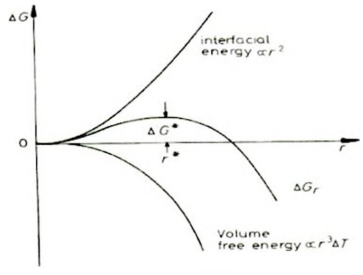

Figure 1.6: *Relationship of surface and bulk energy during nucleation. Results in a critical nucleas size.[19]*

There is an inherent energy barrier which must be overcome in order for the liquid to solidify. Even though the bulk free energy of the solid is lower than the bulk free energy of the liquid($G_S < G_L$), the liquid may not be able to undergo the transition because to create the solid it must first create a nucleated site which also creates an interface between the solid and liquid phases. For small nuclei this interface can raise the energy state more than the conversion to solid lowers the energy and therefore may not be stable.

At any given temperature the liquid has long range disorder and some short range order. (ie. If we were to zoom in to a few atoms it may look as though it were a solid, but upon zooming out we can see that there is in fact, no long-range order.) As the temperature is lowered below the melting point the correlation length over which atoms can spontaneously become ordered grows. These short-range order sites are candidated for nucleation clusters.

When the size of one of these sites is large enough that the decrease in its bulk free energy is larger than the increase in its surface energy, the nucleated grain will grow. This is shown graphically in figure 1.6. If we assume that the nucleation point is a sphere[1] we can calculate the critical radius at which the nucleation is stable by minimizing the Gibbs free energy.

$$\Delta G_r = -\frac{4}{3}\pi r^3 \Delta G_v + 4\pi r^2 \gamma \tag{1.1}$$

Equation 1.1 assumes that the nucleated crystal occurs due to spontaneous fluctuations in the bulk of the liquid. Effective nucleation energies are usually smaller than ΔG_v since nucleation occurs on impurity surfaces(lowering the surface energy which drives the crystal to break apart). The latter process is called heterogeneous nucleation.

Statistically it can be calculated how many nucleated sites will occur at a given undercooling ($T - T_M$). This is done for homogeneous nucleation by determining the energy to spontaneously form a solid sphere equal to the critical radius. Using the theory of statistical mechanics[71, 19, 4] the average number of homogeneous nucleation sites is given by,

$$n_r = n_o e^{(-\frac{\Delta G_r}{k_B T})} \tag{1.2}$$

where n_o is the total number of atoms in the sample.

[1] It is not obvious that this is the case, but results in the minimum surface energy for an isotropic crystal.

1.3.2 Solidification: Pure Materials

Once a system has nucleated and the solid grows into the liquid, the dynamics of the system are determined by the type of material that is being solidified. In the case of a pure material the morphology is determined ultimately by the temperature diffusion within the material, the cooling rate at which it is grown, its surface tension energy and its crystalline anisotropy.

As a solid-liquid interface advances the entropy of the solidifying material drops, resulting in an excess of energy which is released as latent heat of fusion. For a flat interface the heat generated by this transition maintains the interface close to the melting temperature, therefore unless heat is diffused away from the interface solidification will cease. The flux of heat at the interface is related to the latent heat by the flux conservation

$$\alpha_{-}\frac{\partial T}{\partial x}|_{x_{int}^{-}} - \alpha_{+}\frac{\partial T}{\partial x}|_{x_{int}^{+}} = \frac{L}{c_p}V \tag{1.3}$$

where $\alpha\pm$ is the coefficient of thermal conductivity on the solid/liquid side of the interface, L is the latent heat of fusion and c_P is the specific heat at constant pressure, assumed to be constant in both phases here, and V is the local normal velocity of the interface.

The diffusion of heat away from the interface is governed by the heat diffusion equation,

$$\frac{\partial T}{\partial t} = \nabla(\alpha(\vec{x})\nabla T) \tag{1.4}$$

Equations 1.3 and 1.4 control the diffusion of heat from and the corresponding ad-

vancement of, the interface. This allows for a planar interface to advance forward through the liquid. We note that the implicit dependence of V as temperature makes this problem highly non-linear and extremely difficult to solve in real situations.

When the liquid is supercooled ($T < T_M$) the interface advancement can become unstable. This is because if a protrusion of the interface occurs, the tip of this protrusion would cause a steepening of the temperature field in front of it and subsequently heat is diffused away from the interface faster. This leads to an instability that favours growth of the protrusion, and is in fact the origin of dendritic growth.

The effect of curvature in solidifying interfaces leads to a lowering of the local melting temperature(T_{int}) according to the Gibbs-Thompson condition.

$$T_{int} = T_M - d_o^T \kappa - \beta V(t) \tag{1.5}$$

where d_o^T is the thermal capillary length, κ is the local curvature of the interface, and β is a kinetic constant(or function) that is often introduced to account for non-equilibrium effects in rapid solidification.[40, 19, 4]

In real situations d_o^T and β depend on the local crystalline anisotropy of the solidifying grain. Their presence is critical to account for dendritic morphology in solidification[10]. Equation 1.5 corrects for the local increase in free energy due to curved interfaces and coupled with equations 1.3 and 1.4, describes the physics of a solidifying front for a pure material.

1.3.3 Solidification: Binary Alloys

For the case of binary alloys solidification is largely controlled by mass transport(particularly in isothermal conditions). Diffusion of impurities is in turn controlled by the underlying phase-diagram of the particular alloy[2]. The simplest binary-alloy phase diagram is shown in figure 1.7.

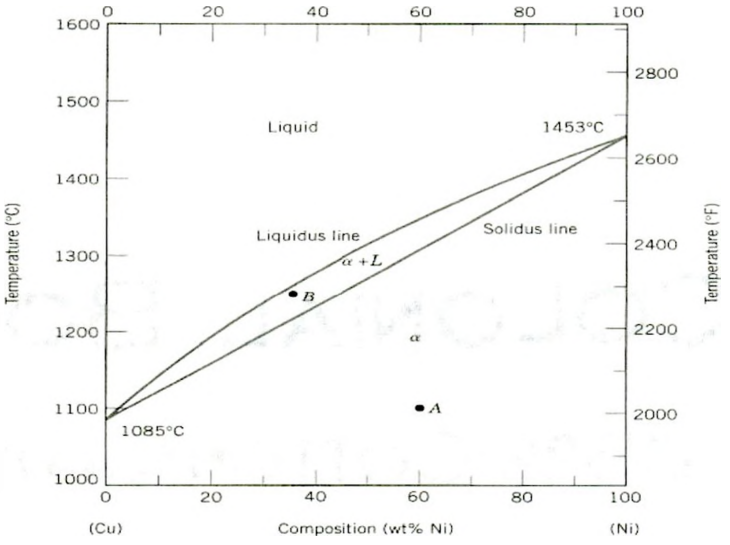

Figure 1.7: *Binary phase diagram for CuNi.[71]*

This diagram is obtained by the minimizing the Gibbs free energy of a Cu-Ni mixture at different temperatures. For a given undercooling(quench) into the co-existence region(point B) solidification proceeds while maintaining concentrations C_S/C_L on either side of the solid/liquid interface, respectively. The flux of solute accross the interface is related to the local normal velocity at the interface and to C_S and C_L by mass conservation,

[2]at least for low to intermediate cooling rates

expressed as

$$\dot{D}_S \frac{\partial C}{\partial x}|_{x_{int}^-} - D_L \frac{\partial C}{\partial x}|_{x_{int}^+} = (C_L - C_S)V \tag{1.6}$$

where D_S is the rate of diffusion in solid and D_L is the rate of diffusion in the liquid. Diffusion of impurities in bulk phases is governed by Fick's law

$$\frac{\partial C}{\partial t} = \nabla(D(\vec{x})\nabla C(\vec{x})) \tag{1.7}$$

where $D(\vec{x})$ is the diffusion function, which depends on $\vec{x}$ since it is different in each phase, and $C(\vec{x})$ is the local impurity concentraion.

The typical thermal diffusion in materials examined in this thesis is four orders of magnitude faster than solute diffusion($\frac{\alpha}{D_L} = 10^4$). As a result the thermal diffusion is assumed to be instantaneous in the material and thermal diffusion may be neglected. This is a reasonable approximation when cooling rate is not too high.

Once again the curved morphology of dendrtitic microstrucures is controlled by the effects of surface tension. In the case of alloy solidification the corresponding Gibbs-Thomson condition is described by

$$\frac{C_{int}(T) - C_{eq}(T)}{\Delta C} = -d_o^C \kappa - \beta V \tag{1.8}$$

where d_o^C is the chemical capillary length, κ is the curvature of the interface, β is the kinetics coefficient and V is the local velocity normal to the interface.

1.3.4 Review of Dendritic Growth

Understanding dendritic growth rates and morphology has been the topic of intense investigation in recent years. The dendrite forms the fundamental unit of solification. As such its properties elucidate much of the fundamental physics of length scale selection in solidification.

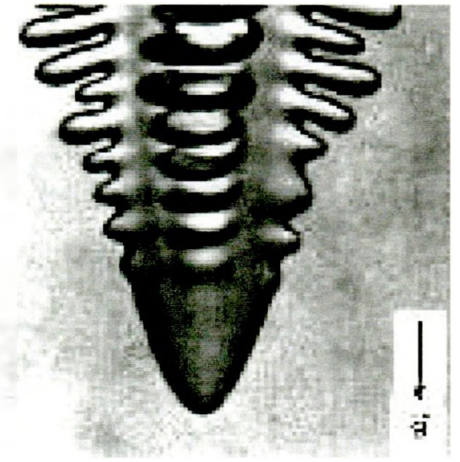

Figure 1.8: *Succinonitrile crystal.[49]*

The process of solidification in metals becomes difficult to study in the laboratory for a number of reasons. Two in particular are quite obvious. Metals reach their liquid state at high temperatures, requiring sophisticated(and expensive) high temperature apparatus to do the study. Another difficulty in using metals is their opacity. It becomes impossible to say anything about the kinetics of dendritic growth when the interface cannot be seen. Materials scientists have turned to organic matertials [27] to study the fundamental nature of solidification. Crystals such as succinonitrile have the advantage of transitioning from the liquid to solid phase near room temperature and the liquid state is transparent(figure 1.8). Such organic materials have been classified as 'organic analogues of metals' due to their similar crystalline behaviour.

Isolated dendritic growth has been characterized by many experiments and phase field simulations.(The phase field method is discussed in chapter 2). The main effort has fo-

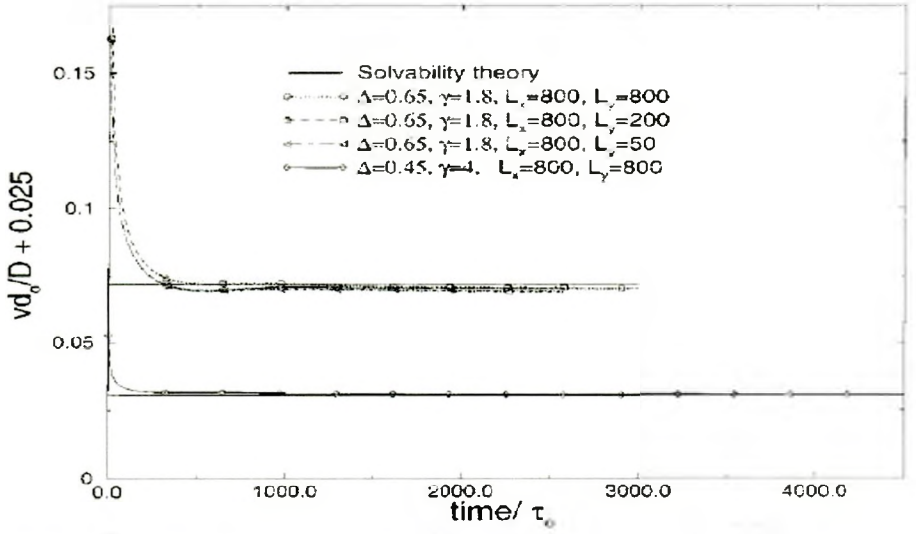

Figure 1.9: *Tip velocities as a function of time for various undercoolings. The points represent phase-field simulations and the horizontal lines are solutions of the stefan problem(ie. solvability theory)[58]*

cused on studying steady-state dendritic growth rates and tip radii. The prevailing theory developed to explain the steady-state properties of dendritic growth in pure materials is the theory of solvability. Solvability theory predicts, from the surface tension anisotropy, a range of allowable tip speeds and radii. Comparisons with experiments[26] have found that the largest such allowable growth rate is selected, corresponding to the smallest allowable tip radius. Figure 1.9 shows a plot of dimensionless tip velocity vs dimensionless time ($\frac{Vd_o^T}{D_L}$vs$\frac{t}{\tau}$) for 2D dendrites grown at 2 different undercoolings where τ is a characteristic time of the simulation. Solvability theory has been found to hold for large undercoolings, but at low undercoolings the growth rates are slow and solvability theory must be abandoned in favour of one that deals with competitive dendritic interactions.[30, 75, 73, 66, 46, 47, 7, 9, 36, 26, 65, 59]

1.3.5 Transient Scaling in Dendritic Growth

When the diffusion fields emanating from different dendritic branches overlap, the solvability theory used to describe dendritic tip evolution is no longer valid. In this case a dynamic theory of dendritic growth is needed. This regime occurs at low undercoolings, such as, for example, in the central, equiaxed, regions of cast ingots.

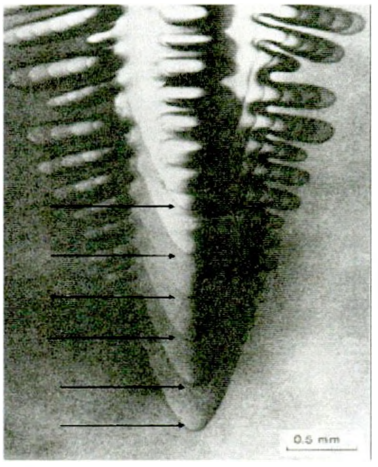

Figure 1.10: *A single dendrite grown in the IDGE project.[51] The crystal tip region is overlayed at different times.*

The dynamics of dendritic growth in the presence of long-range diffusion interactions is defined using the concepts of scaling theory [59]. In this context dendritic morphology has been shown to be self-similar in time. Considering the dendritic crystals in figure 1.10 what this means is that crystals corresponding to different times can be mapped onto a 'univeral' form by a suitable scaling of length scales.

Specifically, by defining the normalized width of a dendrite by

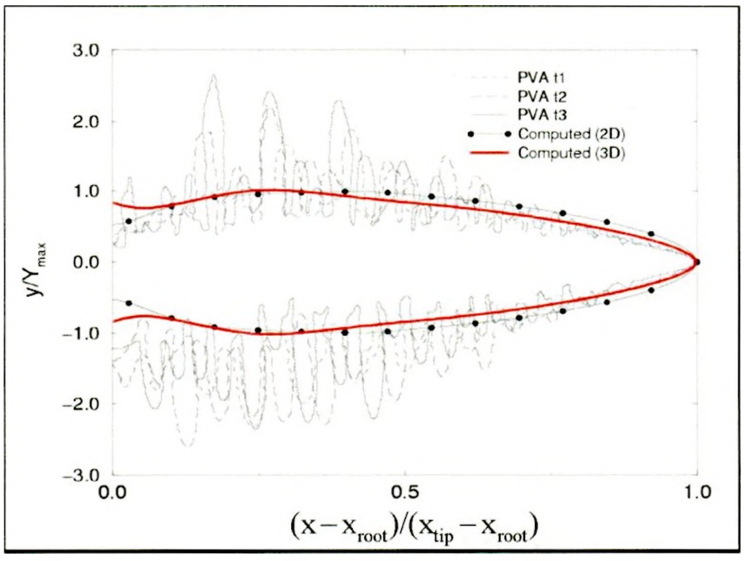

Figure 1.11: *Computed and experimental single dendrite shapes scaled at different times.[59] 3D simulations done with an extension of the model in [59] and are courtesy of Dr. Jonathan Dantzig at the university of Illinois at Urbana-champaign(2002)*

$$y_N = \frac{y}{y_{max}} \tag{1.9}$$

where y_{max} is maximum width of the dendrite measured from the center, and a normalized length given by

$$x_N = \frac{x - x_{root}}{x_{tip} - x_{root}} \tag{1.10}$$

where x_{root} defines the base of the dendrite[3], it has been been found that dendritic structures corresponding to very different times and materials during solidification collapse onto a universal function, a function, shown in 2D and 3D in figure 1.11. As we will see later in this thesis, the scaling concept is a powerful way to describe length scale selection

[3]where it emerges from the solidification nucleus

in other solidification problems.

1.3.6 Directional Solidification

Directional solidification involves the competitive process of many dendrites growing in arrays. Every dendrite has its own solute and temperature field, which interact and overlap with those of other dendrites. Their interaction results in a competition for growth which is dominated by microsegregation and long-range diffusion. This competitive process during growth establishes the final microstructure of the solidified material in a way that cannot be predicted by merely knowing the properties of single dendrites.

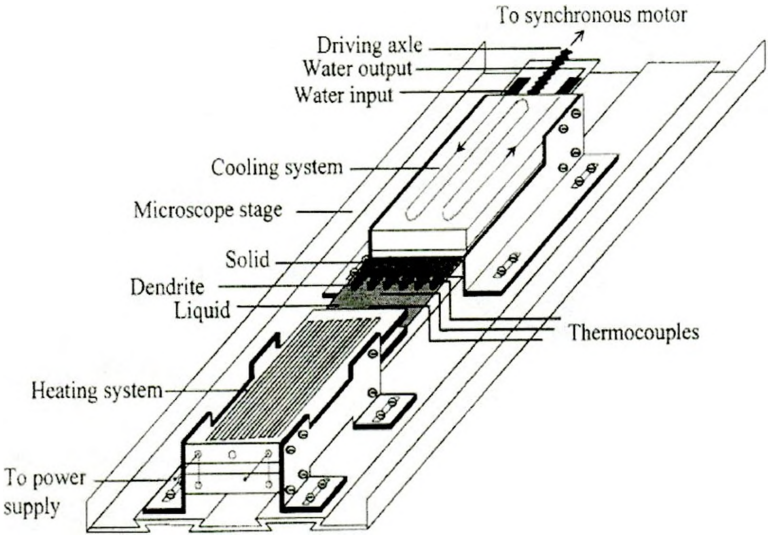

Figure 1.12: *A directional solidification experimental apparatus.[20]*

In directional solidification experiments the arrays of dendrites grown have the same crystalline orientation and at the same cooling rate. The resultant growth will undergo a

transition from planar to dendritic followed by a coarsening into a steady state.[55, 53, 14, 3, 5, 35, 23, 67, 12, 13, 41]

A typical setup to study directional solidification is shown in figure 1.12. A sample is placed in a temperature gradient G, such that the solid is below the melting temperature ($T < T_M$) and the liquid is above it ($T > T_M$), while the interface is at the melting temperature. The solid is slowly pulled into the region below the melting temperature and the interface slowly advances. This results in a relationship of V and G giving a cooling rate VG. Once the cooling rate surpasses a critical value the interface will become unstable and a pattern will initially be selected. This pattern is analagous to the complex dendritic structures found near the walls of cast alloys.

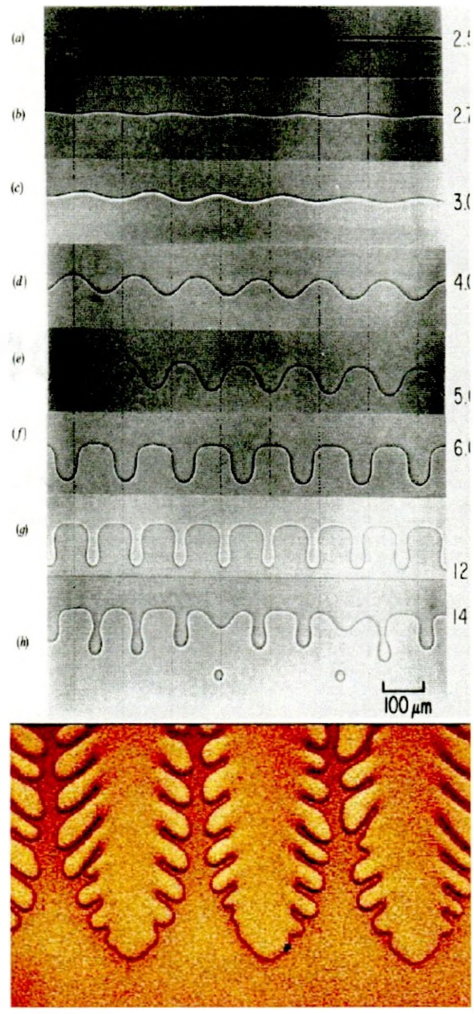

Figure 1.13: *Top: Cell structures under varied cooling rates[23]. Bottom: Dendrite structure(Image from E.Bodenschatz website at milou.msc.cornell.edu/solidification.html)*

Three distinct regions have been classified in the literature. A region where a planar interface exists both at very low cooling rates(Low V if we consider G fixed) and again at very high cooling rates, figure 1.13(a)[42, 31, 64]. As the cooling rate is increased from the lower velocity

regime an instability forms and a cellular pattern emerges as shown in Figure 1.13 (b-h). Increasing the cooling rate further results in a transition from the cellular to dendritic patterns, 1.13 (bottom).

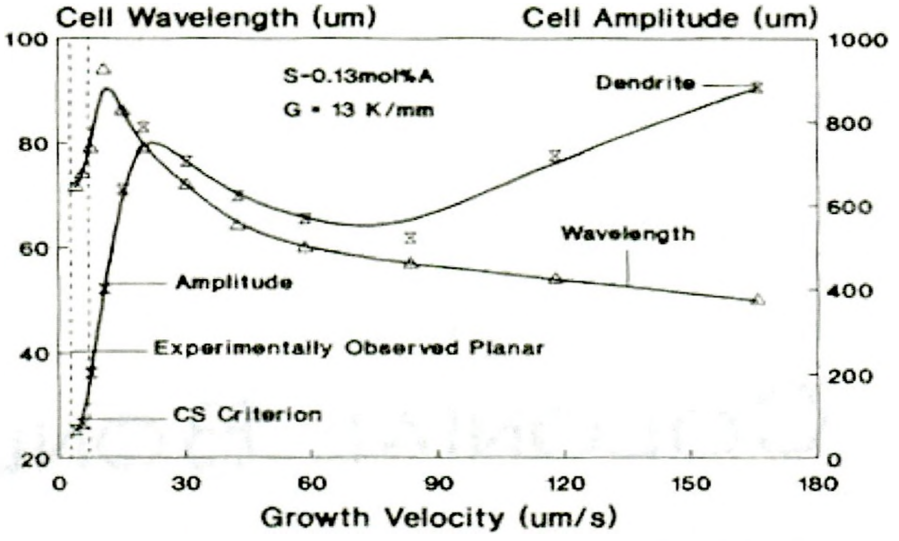

Figure 1.14: *Primary Wavelengths and Amplitudes plotted vs pulling velocity for a succinonitrile experiment[38]*

The 'wavelengths' of selected patterns can be classified as; (1) the primary spacing(the tip to tip separation of the primary dendritic fingers), and (2)the secondary spacing(the tip to tip separation of the side branches). The primary wavelength(λ_1) vs the pulling velocity(V) exhibits a highly non-trivial behaviour. Figure 1.14 shows λ_1 vs V for directionally solidified SCN-Acetone $0.13mol\%$ alloy grown at $G = 13K/mm$. The velocity axis corresponds to cooling rates ranging from $0 - 1K/s$. Changing cooling rates and alloy compositions gives entirely different values of $\lambda_1 vs V$(see chapter 4). [38, 67, 25]

One of the main aims of this thesis will be to characterize the universal features of

$\lambda_1 vs V$, for different material and process parameters(V and G). Before we embark on this investigation, we digress to discuss the nature of solidification instabilities leading to dendritic structure.

1.4 Length Scales in Directional Solidification

1.4.1 The Thermal Length

One of the inherent length scales in solidification processes is the thermal length. The thermal length l_T, is understood by examining the dilute region of a simple binary phase diagram, figure 1.15. Physically l_T corresponds to the length over which the fixed thermal gradient varies between the solidus and liquidus lines, for an alloy concentration C_o.

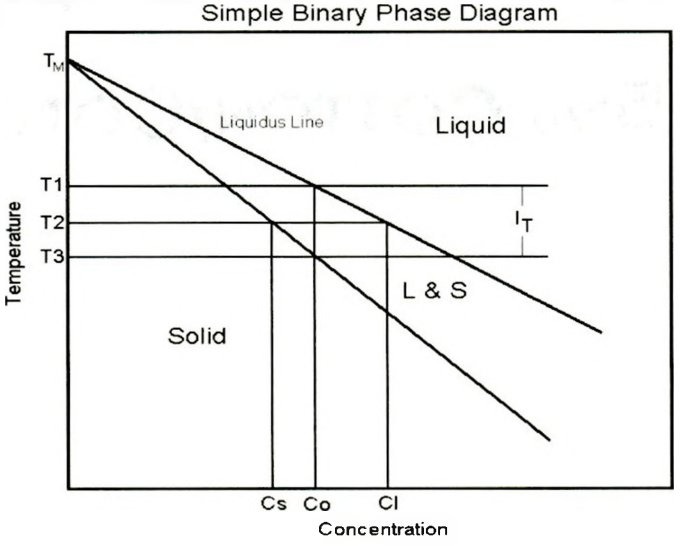

Figure 1.15: *Simple binary phase diagram showing solid and liquidus equilibrium lines. l_T is defined from the temperature separation of these two lines at a concentration C_o*

To quantify l_T consider a planar front advancing at velocity V, and an average alloy concentration C_o. Solute is rejected ahead of the interface as the front advances, maintaining the solid concentration of the interface at $C_s(T)$ and the liquid side concentration at $C_l(T)$. The simple binary phase diagram in figure 1.15 relates these two concentrations by

$$C_L = \frac{C_S}{K} \tag{1.11}$$

where K is the solute partition coefficient.

For a fixed thermal gradient the thermal length is constant and is the physical distance between the temperatures at which the solidus and liquidus lines of the phase diagram cross the concentration C_o, as shown in figure 1.15. Mathematically l_T is thus given by

$$l_T = \frac{m_l C_o^l (1 - K)}{G} \tag{1.12}$$

1.4.2 The Diffusion Length

Another important length scale in alloy solidification is the diffusion length. This length scale characterizes the diffusion of solute away from the interface and is important in the determination of instabilities and the final wavelengths selected.

The difference in the liquid side concentration C_L and the concentration C_o causes the solute to diffuse away from the moving interface producing a concentration profile

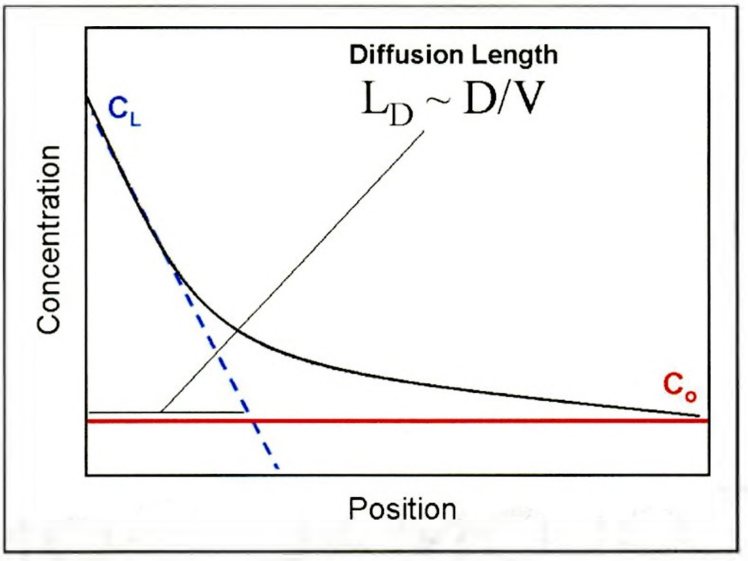

Figure 1.16: *The diffusion length is shown in the above diagram, it is calculated to be the decay length over which most of the rejected impurities are diffused.*

dependent upon both the diffusion coefficient(D) and the local interfacial velocity(V). The form of this concentration profile in steady-state is given mathematically by

$$C_l = C_o(1 + \frac{1-K}{K} e^{-\frac{z}{\frac{D}{V}}}) \tag{1.13}$$

From equation 1.13 the diffusion length is determined to be

$$l_D = \frac{2D}{V} \tag{1.14}$$

1.4.3 Surface Tension and Capillarity

The third length scale relevant to solidification is set by the surface tension energy, and is called the capillary length. This lengthscale is important in establishing the length scale of

dendritic patterns.

Capillarity emerges in the Gibbs-Thomson condition in its connection to surface tension energy and is defined by

$$d_o^T = \frac{\gamma T_M c_p}{L^2} \tag{1.15}$$

for pure materials and

$$d_o^C = \frac{\gamma}{(\Delta C)^2}\frac{\partial \mu}{\partial C} = \frac{L}{\Delta C c_p m_l} d_o^T \tag{1.16}$$

for alloys.

1.5 Planar Instabilities

The transition from planar to unstable solidification fronts is controlled by a competition of the above length scales. These are well documented in the literature[40, 52] and are very important in establishing the main results of this thesis(Chapter 4 and 5).

1.5.1 Constitutional Supercooling

Consider directionally cooling a dilute binary alloy through the phase diagram shown in figure 1.15. As a planar solidification front advances into a thermal gradient G, with a velocity V, the local undercooling, say T_2, of the interface determines the solid side and

liquid side concentrations, C_S/C_L. The liquid-side concentration will diffuse from the interface by equation 1.7 and the planar interface velocity is controlled by equation 1.6.

The planar front will be stable as long as the temperature immediately in front of the interface and the corresponding concentration (equation 1.13) are above the liquidus line of the binary phase diagram. Graphically this is illustrated in figure 1.17. If the gradient of the concentration profile ahead of the interface is steeper than the liquidus line the interface will become unstable. Equating the liquidus concentration, $C_L = (T_M - T)/m_l$, to C_L in equation 1.13 gives

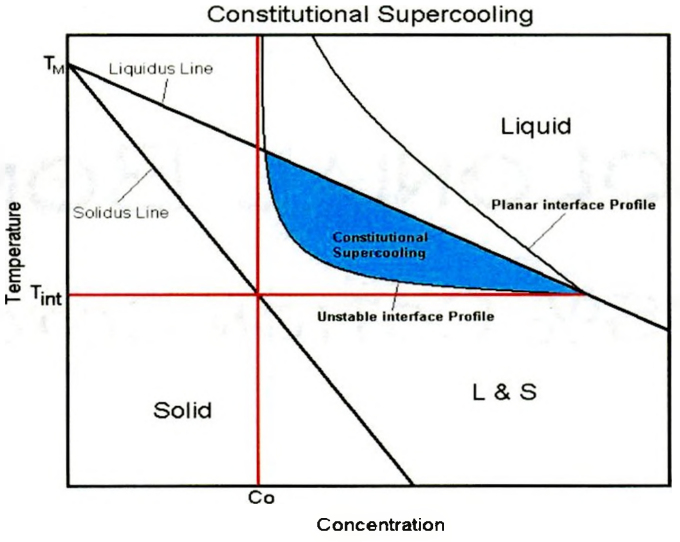

Figure 1.17: *Binary phase diagram overlayed with planar concentration profile, One line shows no constitutional supercooling(CS), thus a planar interface and the other shows CS resulting in an unstable interface.*

$$(Tm - T)/m_l = Co(1 + (1 - K)/K * exp(-z * V/D)) \tag{1.17}$$

The velocity at which the interface becomes unstable can be calculated from the deriva-

tive of equation 1.17 (with respect to the position z) evaluated at the interface(z=0) and $T = Gz + T_{int}$[19]. The resultant derivation establishes the criterion

$$V_C = \frac{DG}{m_l(1-K)C_o^l} \tag{1.18}$$

This is the constitutional supercooling criterion for the emergence of dendritic instabilities. Note that it is equal to $l_D/l_T = 2$. At this level of description constitutional supercooling does not incorporate surface tension effects, and as such is only valid at very low cooling rates.

1.5.2 Mullins-Sekerka Theory

The Mullins-Sekerka instability theory incorporates surface tension effects and predicts the selected length scale that initially emerges when the cooling rate exceeds a critical value. We note that the traditional constitutional supercooling describes when the interface will become unstable, but it tells nothing of the emerging length scales of patterns that emerge. Moreover by neglecting the effects of surface tension, it underestimates the velocity(cooling rate) at which the interface becomes unstable.

The Mullins-Sekerka theory is a linear-stability analysis which examines the amplification of wavelengths promoted by thermal fluctuations of a stable solid/liquid interface. Once a critical cooling rate(pulling velocity) is surpassed some wavelengths are slowly amplified, while others decay. One particular wavelength is amplified more than any other and

at very low cooling rates this fastest growing wavelength is given by

$$\lambda_{MS} \propto \sqrt{l_D d_o} \tag{1.19}$$

This is the wavelength that is amplified the most and thus it out grows all other wavelengths becoming the initially selected wavelength.[40, 23, 52] Indepth calculations of the Mullins-Sekerka instabilities are given in [40] for different interface shapes and processes.

The calculation of the amplification rate for the directional solidification of a binary alloy is beyond the scope of this thesis but its details are presented in Ref[40]. The wavelength selection used in this thesis makes the following assumptions:

1)Solute Diffusivity vanishes in the solid phase($D_S \rightarrow 0$).

2)Latent heat at the interface is instantly diffused away.

3)The thermal conductivities in the solid and liquid phases are the same.

The amplification rate ω_k of a given wave vector(ie frequency) $k = 2\pi/\lambda$, for these assumptions is found to be

$$\omega_k = (ql_D - 2 + 2K)(1 - \frac{1}{\nu} - \frac{1}{2}V(kl_D)^2 - \frac{2K}{ql_D - 2 + 2K})\frac{2D_L}{l_D^2} \tag{1.20}$$

where $q = \frac{1}{l_D}(1 + \sqrt{1 + (kl_D)^2})$, l_D is the diffusion length, k is a wave frequency, $\nu = 2l_T/l_D$ is the stability parameter, D_L is the solute diffusion constant in the liquid, K is the partition coefficient and V is the interfacial velocity.

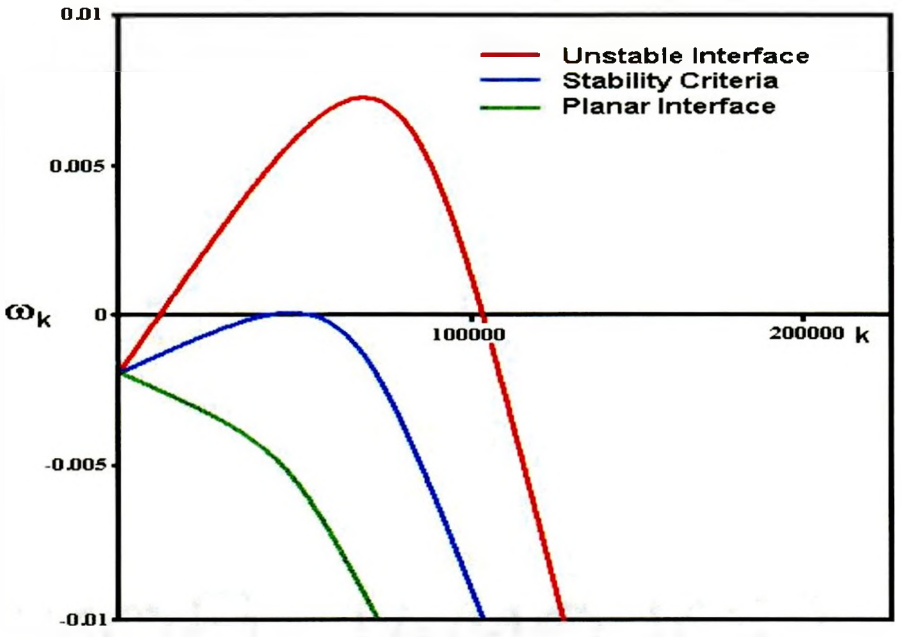

Figure 1.18: *Amplification rate(ω_k) plotted vs wave number $k = 2\pi/\lambda$ for 3 difference velocities. The cases of an unstable interface, the stability criteria and a stable interface are all shown.*

ω_k vs k is illustrated for 3 different velocities in figure 1.18. The maxima represents the frequency with the maximum amplification rate. If the rate at any frequency is positive the interface becomes unstable and perturbations of this frequency grow. This fastest growing frequency can be extracted by solving,

$$\frac{d\omega_k}{dk} = 0 \tag{1.21}$$

The dominant wavelength $\lambda_{dom} = 2\pi/k_{dom}(V)$ is calculated by solving equation 1.21 for k as a function of V, producing $k_{dom}(V)$. Increasing the instability parameter ν(figure 1.18 lower to upper lines) results in the maxima of the curve to increase and cross $\omega_k = 0$,

this is the criteria for planar stability for the Mullins-Sekerka instability analysis.

Chapter 2

Phase Field Method

Modelling solidification with the sharp interface model poses significant problems of computational and fundamental practicality [63, 16]. The sharp interface model applies boundary conditions at an infinitely sharp interface. To simulate solidification in this approach the interface must be explicitely tracked. In simple cases this can be done with interface tracking algorithms, but with complicated growth topologies the problem of interface tracking becomes unmanageable in 2D and 3D. Also, the sharp-interface model doesn't make a direct connection to the free energy of a solidifying system, making it difficult to extend to more complex situations[1].

In this chapter we will illustrate the phase field method, focusing on the specific model

[1]For example when elasto plastic effects are incorporated into solidification or certain solid-state transformations, it is not obvious what the "sharp-interface" model should be and one needs to begin from the fundamental thermodynamics of the problem.

for alloy solidification that we use in our work.

2.1 Phase Field - Pure Material

We begin our illustration of the phase-field method by examining the simple case of solidification of a pure material.[18, 27, 37, 54, 56, 60, 68] Two fields are needed to describe the solidification process using the phase field approach; the thermal field and a field of the "order parameter", a function which describes the solid, liquid and the phase boundary between them. The order parameter, ϕ, is defined such that it has a constant value in the solid phase($\phi = 1$) and a continuous transition to the liquid phase($\phi = -1$) over a finite interface width W, as illustrated in figure 2.1. The growth of the interface is manifested as a propagation of the $\phi - field$ as illustrated in figure 2.2.

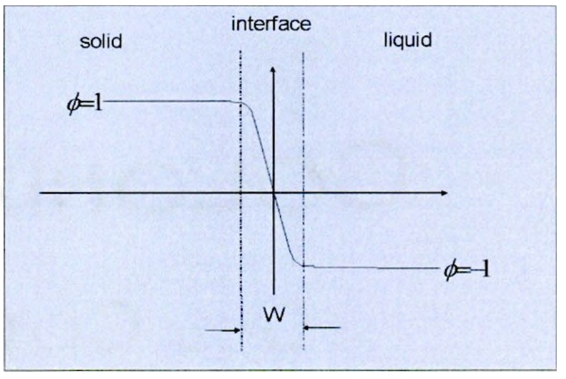

Figure 2.1: *Schematic of an interface of the phase field in 1D. The solid phase has a value of $\phi = 1$, a smooth transition through the interface and a value of $\phi = -1$ in the liquid.*

The phase field method begins with the free energy(F) of the solid-liquid system expressed in terms of the temperature and the order parameter ϕ. This is given by

$$F = \int (|W(\vec{n})\nabla\phi|^2 - \frac{\phi^2}{2} + \frac{\phi^4}{4} - \lambda UP(\phi))dV \tag{2.1}$$

Where $U = (T - T_M)/(L/c_p)$ is the dimensionless temperature field, T_M is the melting temperature, L is the latent heat of fusion and c_p is the specific heat at constant pressure. The constant λ is proportional to the inverse of the nucleation energy $\Delta G_{NUC}{}^2$.

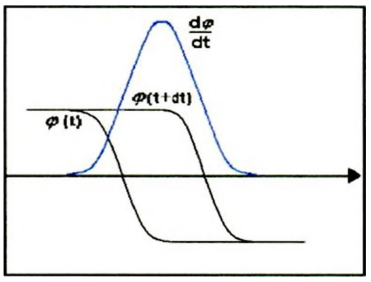

Figure 2.2: *Schematic of an advancing interface. The form of the interface shape changes little, but advances mostly as a propagating front.*

$|W(\vec{n})\nabla\phi|^2$ controls the surface tension energy, and $W(\vec{n})$ is the interface thickness. The dependence of W on $\vec{n}$, the local normal to the solid-liquid interface[33, 74, 22, 34], is used to model surface tension anisotropy. The function $P(\phi)$ is an algebraic function[3] of ϕ, and is required to take on the limits $P(\phi = \pm 1) = \pm 1$ and $P'(\phi = \pm 1) = 0$. In this thesis $P(\phi) = \phi - \frac{\phi^3}{3} + \frac{\phi^5}{5}$. The function $h(\phi) = -\frac{\phi^2}{2} + \frac{\phi^4}{4} - \lambda U P(\phi)$ represents the normalized bulk free energy density. Its form is shown in figure 2.3, which illustrates the relative changes of the free energy between the bulk solid($\phi = +1$) and liquid($\phi = -1$) as the temperature changes. For a known temperature field $U(\vec{x}, t)$, the equation of motion for ϕ is given by

$$\frac{\partial \phi}{\partial t} = -\frac{\delta F(\phi, U, x)}{\delta \phi} = W^2 \nabla^2 \phi - \phi + \phi^3 - \lambda U(\vec{x}, t)(1 - \phi^2)^2 \qquad (2.2)$$

[2]In cases where we are not concerned with modeling nucleation kinetics but, rather, the kinetics of dendritic microstructure, λ can be treated as a free parameter

[3]It can be shown rigorously that in the limit when $W \to 0$(i.e. a sharp-interface limit of the phase-field model) the form of $P(\phi)$ is insignificant and all that enters the picture are its limits[15, 16, 17, 22, 33, 74]

For this overview we have assumed W, the interface width, is constant to keep the mathematical development simple here. The expression $\delta F/\delta\phi$ is a variational derivative of the integral expression F as the function ϕ.

The dimensionless temperature $U(\vec{x},t)$ is coupled to the dynamics of $\phi(\vec{x},t)$ through a modified heat diffusion equation

$$\rho c_p \frac{\partial T}{\partial t} = \nabla(K(\phi)\nabla T) - \frac{L}{2c_p}\frac{\partial \phi}{\partial t} \qquad (2.3)$$

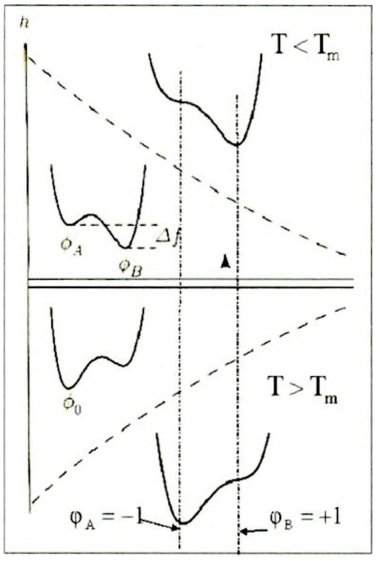

Figure 2.3: *The double well is defined everywhere. Top: $T < T_M$ The well shifts towards the solid. Bottom: $T > T_M$ The well shifts to the liquid.*

The last term represents a "blip" of latent heat released at the advancing solidification front. Its form is related to $\phi(\vec{x},t)$ as illustrated in figure 2.2. It should be noted that in the limit when the interface width $W \to 0$, the above solidification model reduces exactly to the sharp interface model of a pure material as discussed in chapter 1.[15, 22, 33, 74, 17] A derivation of this result is beyond the scope of this thesis.

Phase-field models of solidification and solid-state transformations have been developed to capture the dynamics of microstructure formation. Figure 2.4 illustrates the versatility of the phase field method in the study of phase transformations, for example, the morphological changes of single crystals(left), the effects of heat convection in solidification(middle) and the study of spinodal decomposition(right)[1, 33, 2, 61, 11, 75, 66, 48, 7].

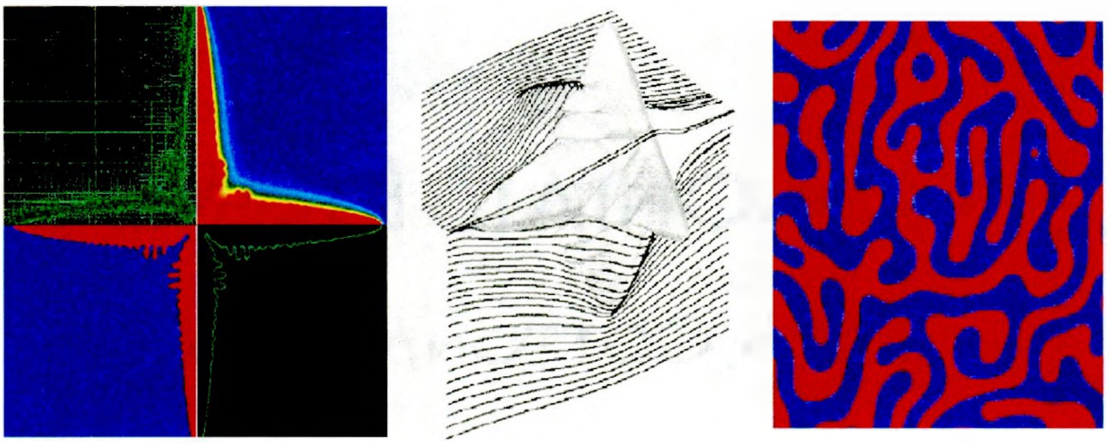

Figure 2.4: *Left:A 2D pure dendrite grown with the thermal Phase Field[59] Middle:Convective effects tested on 3D dendrites[30] Right:Spinodal Decomposition using Phase Fields* pmc.polytechnique.fr/mp/Recherche.html

2.2 Phase Field - Binary Alloy Solidification

Analogously to the phase field for the pure material, we now illustrate the model for binary alloy solidification used in the simulations completed in this thesis. This model describes solidification of a dilute binary alloy with a partition coefficient K and couples an order parameter ϕ to a concentration field C. As in the pure material $\phi(\vec{x})$ is constructed to take on the values $\phi = 1$ in the solid phase, $\phi = -1$ in the liquid phase and is interpolated continuously between these states in the interface region.

The free energy density of a dilute binary alloy in terms of the order parameter ϕ, the concentration C, and the temperature T, is given by

$$F = \int |W(\vec{n})\nabla\phi|^2 + f_D(\phi) + f_{AB}(\phi, C, T)]dV \tag{2.4}$$

where $|W(\vec{n})\nabla\phi|^2$ is as described in the case of a pure material, $f_D(\phi) = H(-\frac{\phi^2}{2} + \frac{\phi^4}{4})$ is a double well potential with H proportional to the nucleation energy barrier and f_{AB} is the free energy of mixing in either phase, given by

$$f_{AB} = f_A(T_M) - \Delta TS(\phi) + \frac{RT_M}{\nu_o}(ClnC - C) + \epsilon(\phi)C \tag{2.5}$$

where,

$$\epsilon(\phi) = \epsilon + \frac{\Delta\epsilon}{2}g_1(\phi) \tag{2.6}$$

$$\Delta\epsilon = \epsilon_S - \epsilon_L$$

$$\epsilon = \frac{\epsilon_S + \epsilon_L}{2}$$

and

$$S(\phi) = \frac{S_S + S_L}{2} - \frac{L}{2T_M}g_2(\phi) \tag{2.7}$$

is the entropy as a function of phase.

The function $f_A(T_M)$ is the free energy of the pure material, $\Delta TS(\phi)$ is the entropic contribution due to a phase difference and temperature difference(ΔT) from the melting temperature. The term $\frac{RT_M}{\nu_o}(ClnC - C)$ is the contribution due to the entropy of mixing and $\epsilon(\phi)C$ is the enthalpy contribution as a function of phase. R is the gas constant, T_M is the melting temperature, ν_o is the unit volume, S_L and S_S are the liquid and solid entropies

respectively, ϵ_S and ϵ_L are the bond energies of solid and liquid states and g_1 and g_2 are functions for interpolating ϕ between solid and liquid states where the limits of $g_{1,2}(\phi = \pm 1) = 1$ and $g'_{1,2}(\phi = \pm 1) = 0$.

The diffusion of solute is given by the generalized Fick's law

$$\frac{\partial C}{\partial t} = \nabla(M(\phi, C)\nabla\mu) \tag{2.8}$$

where $M(C, \phi) = \frac{\nu_o}{RT_M} D_L q(\phi) C$ in the dilute limit, $q(\phi)$ is a function that interpolates the mobility(M) between its solid and liquid values and μ is the chemical potential given by

$$\mu = \frac{\delta F}{\delta C} = \frac{RT_M lnC}{\nu_o} + \bar{\epsilon} + \frac{\Delta\epsilon}{2} g_1(\phi) \tag{2.9}$$

the corresponding equation for ϕ is given by the variational derivative as in the pure model

$$\tau \frac{\partial \phi}{\partial t} = -\frac{\delta F}{\delta \phi} = W^2 \nabla^2 \phi - H(\phi - \phi^3) - \frac{\partial f_{AB}}{\partial \phi} \tag{2.10}$$

where $\tau = 1/Hk$ and $\partial f_{AB}/\partial\phi$ is given by

$$\frac{\partial f}{\partial \phi} = \frac{C_l \Delta\epsilon(1 - K)}{2lnKC_o(\phi)} (C_o(\phi) - C(x)) g'_2(\phi) \tag{2.11}$$

where the concentration in the interface is described by

$$C_o(x) = C_o^l e^{\frac{lnK}{2}(1+g_1)(\phi_o(x))} \tag{2.12}$$

which is the steady state concentration profile and $\phi_o(x)$ is the form of the phase-field across a stationary solid/liquid interface, given by the solution of

$$W^2 \frac{d^2\phi_o}{dx^2} - \frac{\partial f}{\partial \phi_o} = 0 \tag{2.13}$$

$C_o(x)$ is constructed by noting that the chemical potential, equation 2.9, is constant(μ_{eq}) across the solid-liquid interface, ie,

$$\mu_{eq} = \frac{RT_M}{\nu_o} lnC_o + \epsilon(\phi_o) \tag{2.14}$$

manipulating equation 2.14 and substituting equation 2.6 gives equation 2.12.

The binary phase diagram is constructed from the chemical potential, equation 2.14. At equilibrium the chemical potential on the solid side of the interface is found to be

$$\mu_{eq} = \frac{RT_M}{\nu_o} lnC_S + \epsilon(1) \tag{2.15}$$

while on the liquid side it is given by

$$\mu_{eq} = \frac{RT_M}{\nu_o} lnC_L + \epsilon(-1) \tag{2.16}$$

Equation 2.15 and 2.16 immediately produce the partition coefficient,

$$K = \frac{C_S}{C_L} = e^{-\frac{\Delta_\epsilon \nu_o}{RT_M}} \tag{2.17}$$

while applying the double tangent construction to the bulk free energy, equation 2.5,

$$f_{AB}(-1, C_L) - f_{AB}(1, C_S) = \mu_{eq}(C_L - C_S) \tag{2.18}$$

The liquidus slope of the characteristic dilute limit of a simple binary phase diagram is found to be

$$m_l = -\frac{RT_M^2(1-K)}{L\nu_o} \tag{2.19}$$

Using the identity(requires much algebra),

$$g_1' \frac{C - C_o}{C_l} = \frac{-2(1-K)^2}{lnK}(e^U - 1)g_2' \tag{2.20}$$

equation 2.10 is recast in the form of the phase equation similar to that in [32], ie,

$$\tau \frac{\partial \phi}{\partial t} = W^2 \nabla^2 \phi + \phi - \phi^3 - \frac{\lambda}{1-K}(e^U - 1)g_2'(\phi) \tag{2.21}$$

where

$$\lambda = \frac{RT_M(1-k)^2 C_o^l}{\nu_o H} \tag{2.22}$$

In our work we have used $g_2' = (1 - \phi^2)^2$.

In directional solidification temperature is modeled using a thermal gradient through which the interface is pulled at a velocity V. Since the thermal diffusion is orders of magnitude greater than the solute diffusion(which governs the rate of dendritic growth) $\frac{\alpha}{D_L} \approx 10^4$ the thermal gradient is taken to be constant[40]. This is often called the "frozen field" approximation. This thermal field is defined by

$$T = T_o + G(z - Vt) \tag{2.23}$$

where G is the frozen thermal gradient, z is the distance along the growth direction from a point at which $T = T_o$ and which moves with velocity.

For convenience we work in units where space is rescaled by W, time by τ and temperature by $m_l(1 - K)C_o$ where C_o is the initial alloy concentration, m_l is the liquidus slope and k is the partition coefficient. In these units the temperature field is given by

$$\theta = (1 - K)(z - Vt)/l_T \tag{2.24}$$

and the dimensional pulling velocity is

$$V = V_R\tau/W \tag{2.25}$$

where V_R is the real pulling velocity. The dimensionless diffusion constant is given as,

$$D = D_L\tau/W^2 \tag{2.26}$$

where D_L is the diffusion constant in the liquid. Diffusion in the sample is controlled by

$$\bar{D} = Dq(\phi) \tag{2.27}$$

where,

$$q(\phi) = \frac{(1-\phi)}{1+K-(1-K)\phi} + \frac{(1+\phi)\xi}{2} \tag{2.28}$$

and where $\xi = D_S/D_L = 10^{-4}$.

Surface tension anisotropy is incorporated into the phase-field model using fourfold symmetry and is specified in terms of $\vec{n} = \nabla\phi/|\nabla\phi|$, the unit normal to the interface. The form of this anisotropy is

$$A(\vec{n}) = [1-3\epsilon_4][1+\frac{4\epsilon_4}{1-3\epsilon_4}((n_x)^4+(n_y)^4)] \tag{2.29}$$

where ϵ_4 is the anisotropy constant. The anisotropic interface width is defined as $W_o(\vec{n}) = W\,A(\vec{n})$ and the characteristic time $\tau_o(\vec{n}) = \tau A^2(\vec{n})$ [33, 57, 74, 32]. Anisotropy appears in both τ_o and W_o to make the interface kinetics term $\beta = 0$ in the sharp interface limit.

In non-dimensional units the final form of the phase-field model[32] we use is given by the solute diffusion equation,

$$\frac{\partial C}{\partial t} = -\nabla \cdot \vec{j} \tag{2.30}$$

and the phase field equation,

$$\begin{aligned} A^2(\vec{n})\frac{\partial \phi}{\partial t} &= \vec{\nabla} \cdot (A^2(\vec{n})\vec{\nabla}\phi) + \phi(1-\phi^2) \\ &- \frac{\lambda}{1-K}\left(e^U + \theta - 1\right)(1-\phi^2)^2 \\ &+ \frac{1}{2}\vec{\nabla} \cdot \left[|\nabla\phi|^2 \frac{\partial A^2(\vec{n})}{\partial(\vec{\nabla}\phi)}\right] \end{aligned} \tag{2.31}$$

where $e^U = 2(C/C_l^o)/(1+k-(1-k)\phi)$ and flux $\vec{j} = -DCq(\phi)\nabla u - a_t C_l^o(1-k)e^{\mu}(\partial_t\phi)\vec{n}$ is a solute anti-trapping term for when $d_o \approx w_o$

The free phase field coefficients W, τ, λ and the anti-trapping flux coefficient a_t are all inter-related through an asymptotic analysis [32], which maps the phase-field model onto the sharp interface limit stated earlier in this thesis:

(1) solute diffusion in the bulk phases, Fick's Law,

(2) flux conservation at phase-boundaries, and

(3) the Gibbs-Thomson condition

Establishing a connection between the phase field model and the sharp interface limit leaves us with only one free parameter, λ, which doesn't influence the final results. Solving the phase field equations in the limit of local interface equilibrium[4], ie $\beta = 0$, the rela-

[4]The value for interface kinetics coefficient β is under investigation, for small interface velocities the approximation of $\beta = 0$ is valid

tionships between the phase field coefficients and the corresponding material constants are obtained. These are given here without proof. The capillary length d_o^C,

$$d_o^C/W \approx 0.8839/\lambda \tag{2.32}$$

the solute diffusion coefficient D,

$$D \approx 0.6267\lambda \tag{2.33}$$

and the anti trapping coefficient a_t,

$$a_t = 1/(2\sqrt{2}) \tag{2.34}$$

Applying this model allows for the simulation of competative dendritic systems. Shown in figure 2.5 is the time evolution of the concentration field for a dendritic array with a gradient $G = 9.75K/mm$ and a pulling velocity $V = 30\mu m/s$. Microsegregation of solute in the solid takes place between the dendrites as the dendrites grow.

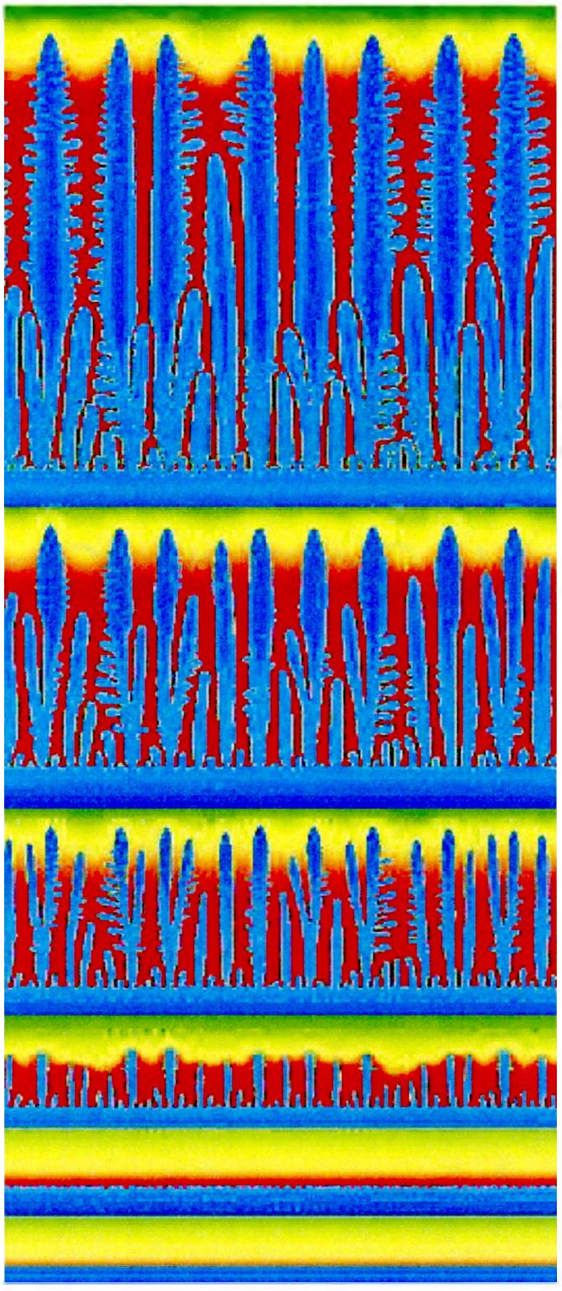

Figure 2.5: *Phase field simulation of the concentration field for directional solification of the binary alloy PVA-0.813%ETH in a gradient* $G = 9.75K/mm$ *and* $V = 30\mu m/s$ *at times 6.7s, 8.7s, 10.6s, 13.5s, 18.3s and 28.9s. Blue is low concentration and red represents a high concentration.*

Chapter 3

Computational Methods

3.1 Phase Field and Multiscaling

The simplest method of computing time dependent solutions of the phase field equations described above is to solve the PDEs using finite differencing methods to calculate the gradients and to update each nodal point in a uniform mesh by explicit timestepping. The interface width of a solidifying material using the phase field method is generally on the order of 10^{-9} to 10^{-8}m while the final dendritic structure can be on the order of 10^{-4}m. As much as 6 orders of magnitude difference occurs in the growth of dendritic structures and even in the 2D case this can generate a static uniform mesh with as many as 10^{12} nodal points. This results in unrealistically long computation times and memory management becomes almost impossible. What is required is a method which can dynamically deal with multiscale problems.

3.2 Dynamic Adaptive Grid Method

The dynamic adaptive grid method alters the numerical mesh resolution dynamically as the computation is advanced through time. This allows the system to resolve to needed accuracy in regions of importance and to save computation time and memory by unresolving where such accuracy is not required. In solidification, regions of importance means regions near the solid/liquid interface, where the phase transition is occuring. This principle applies to any problem where

$$\frac{interfacelength(or Area)}{domain area(or Volume)} << 1 \tag{3.1}$$

such as in solidification and solid state transformations.

The dynamic adapative grid method creates a non-uniform mesh that automatically places higher densities of nodal points near moving interfacees and much lower densities of nodal points away from the moving interfaces. This unstructured numerical grid is represented as a finite element mesh.

The dynamic adaptive grid adjusts the local resolution at an increment of time($t + \Delta t$) by use of a function which estimates the local error(based on fluxes of the fields) on the current mesh at time(t). The error estimator we use is given by

$$E = |\nabla \phi| + \gamma |\nabla U| \tag{3.2}$$

where ϕ is the phase, U is the temperature or solute concentration and γ is a prefactor

to set the importance of the slower varying diffusion field in the error calculation. If the local error is too large at the current resolution, the grid is further refined locally.

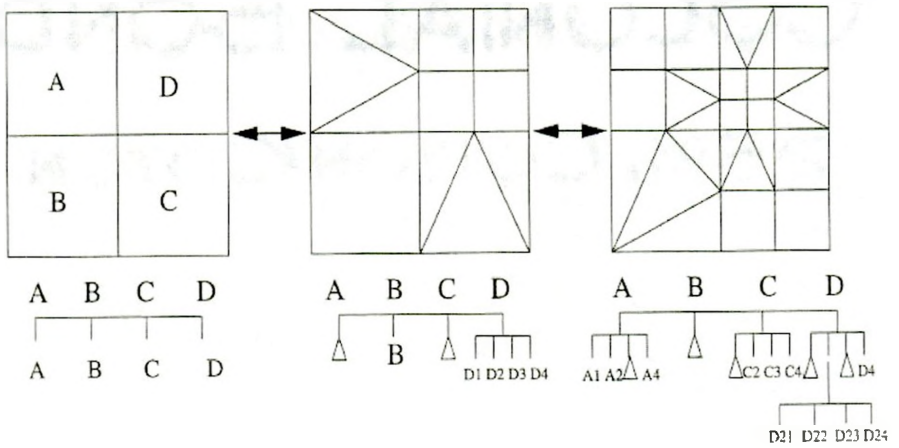

Figure 3.1: *Pictoral diagram of a quad-tree structure used in adaptive meshing. An element splits and creates 'children' beneath it in the tree structure. If any element has no children it is 'active'[58]*

Dynamic adaptive meshing is applied to an FEM mesh of quadrilateral and triangular elements. Square elements are used for ease of refinement and for regular interpolation of the fields, but nodal mismatches can occur between elements of differing resolutions. This is resolved by the addition of linear triangular elements used to bridge these elements. Figure 3.1 [58] shows a sequence of successive grid refinements and the associated data-structure used to code the refinement procedure numerically.

Figure 3.2 illustrates the dynamic adaptive mesh in action by showing the mesh for 5 different times. At $t = 0.96s$ the grid is symmetrical around the interface with little alterations and at $t = 9.6s$ the interface has broken up and primary branches have emerged, the mesh has adapted to maintain the grid resolution at the interface. Times $t = 11.5s$ and

$t = 14.4s$ show the continued growth of the dendrites and the emergence of sidebranches, finally $t = 29.8s$ the merger of side branch interfaces results in some unresolving of the mesh.

3.3 Application to the Phase Field

Equations 2.30 and 2.31 are solved on the dynamic adaptive grid. The equations are discretized using a linear isoparametric formulation of the finite element method[62]. Time integration of the discrete equations is done explicitly. The phase-field model was simulated in 2D with zero-flux boundary conditions in both C and ϕ [57, 74]. All direction solidification simulations begin with a planar solidification front which is initialized with a small-amplitude random perturbation. To reach convergence the model was run with a minimum grid spacingof $dx_{min} = 0.39$ in all cases. Explicit time integration was used, with a time step $dt = 0.008$ as in Ref[32]. We used various values of λ, which merely set the length and time scales of our simulations. Data from different λ values can be rescaled onto one another.

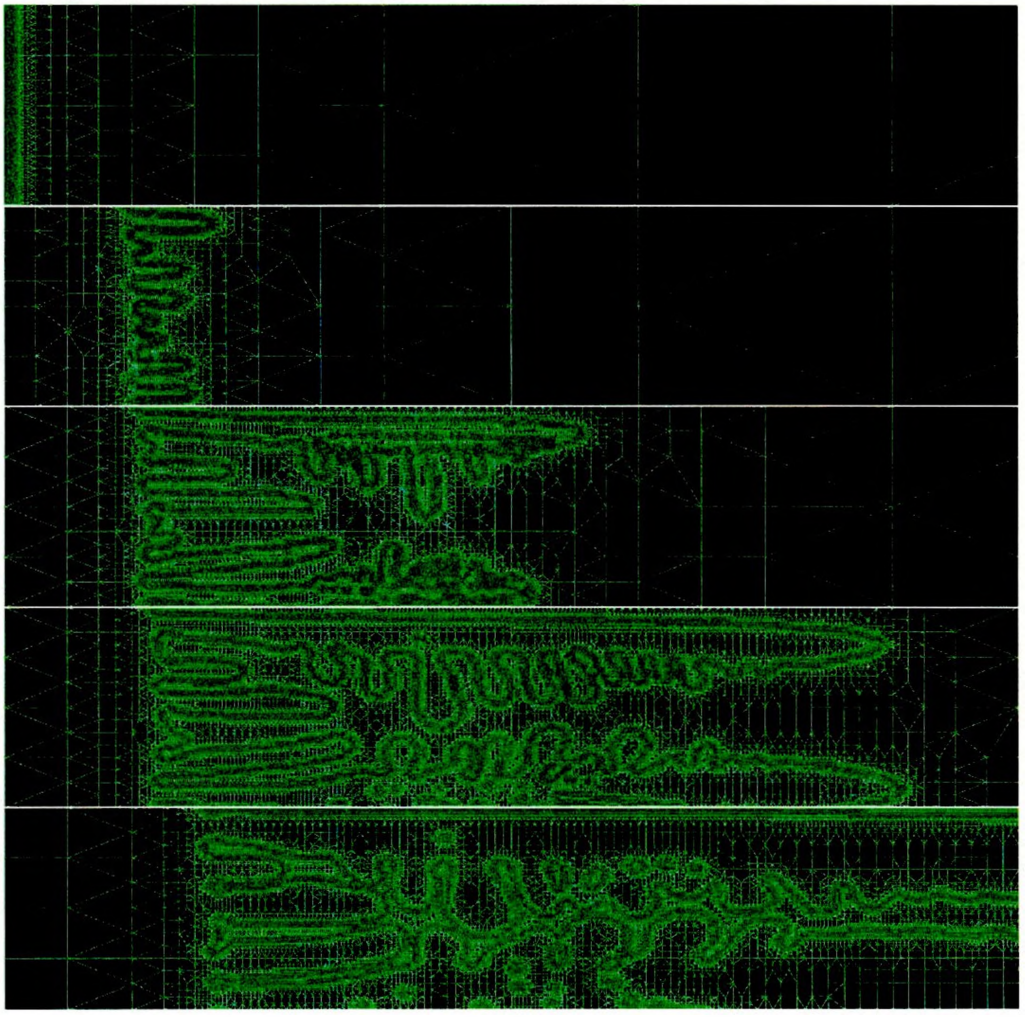

Figure 3.2: *Dynamic Adaptive Grid for directional solification in a gradient* $G = 9.75K/mm$ *and* $V = 30\mu m/s$ *at times 0.96s, 9.6s, 11.5s, 14.4s and 29.8s*

Chapter 4

Dendrite Spacing Selection in Directional Solidification

Chapters 4 and 5 report the main results of this thesis. The goal of this thesis is to find a material-independent scaling relationship for primary dendritic spacing in directional solidification as a function of the material and process parameters. This chapter overviews experimental data previously published by Dr. Jack Kirkaldy's group at McMaster University [38, 42] for primary wavelength selection in directional solidification and reports on new phase field simulations conducted by myself on directional solidification. We simulated directional solidification in two dimensions, and compared our results to Dr. Kirkaldy's data, which was also effectively two dimensional[1].

[1]By avoiding capillary effects Dr. Kirkaldy's experimental data features a distinct absence of 3D side branching, indicating 2D dendritic growth

As in many previous directional solidification experiments[69, 8, 23, 6, 44, 45, 43, 70, 31, 38, 42, 67, 12, 13], the experimental data of [38, 42] were done using alloys of pivalic acid(PVA) and succinonitrile(SCN). The alloying elements were salol, acetone and ethanol. Figure 4.1 illustrates a simplified schematic of the aparatus used to run the diectional solidification experiments of [38, 42]. The experiments are run by creating a solid-liquid planar interface[2] between two parallel plates. A temperature gradient G, is applied across the interface and the material is pulled at a velocity V through the gradient as shown in figure 4.1.

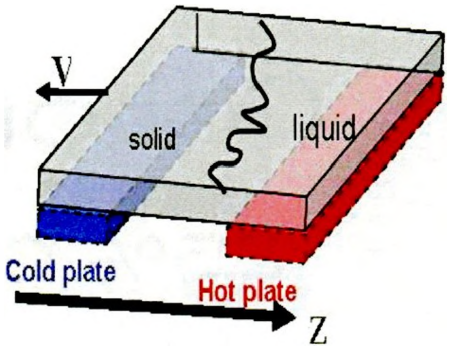

Figure 4.1: *Diagram of directional solidification, cold and hot plates create a temperature gradient and the interface is pulled toward the cold side.*

Our model simulates the above setup, as the experiments, except that the gradient is pulled toward the hot plate with a velocity V.

4.1 Survey of Experiments

This section summarizes experimental data of primary wavelength(λ_1) selection previously published by Dr. Jack Kirkaldy[38, 42]. These directional solidification experiments are run between parallel plates in which 3D effects are minimized by using a film thickness

[2]The interface is rough on the scale of nanometers

of $55\mu m << l_D$. An initial planar front is pulled back into the temperature gradient G at a velocity V. Three sets of λ_1 vs V have been published in refs [38, 42], pivalic acid alloyed with ethanol(PVA-ETH), succinonitrile with acetone(SCN-ACE) and sucinonitrile with salol(SCN-SAL).

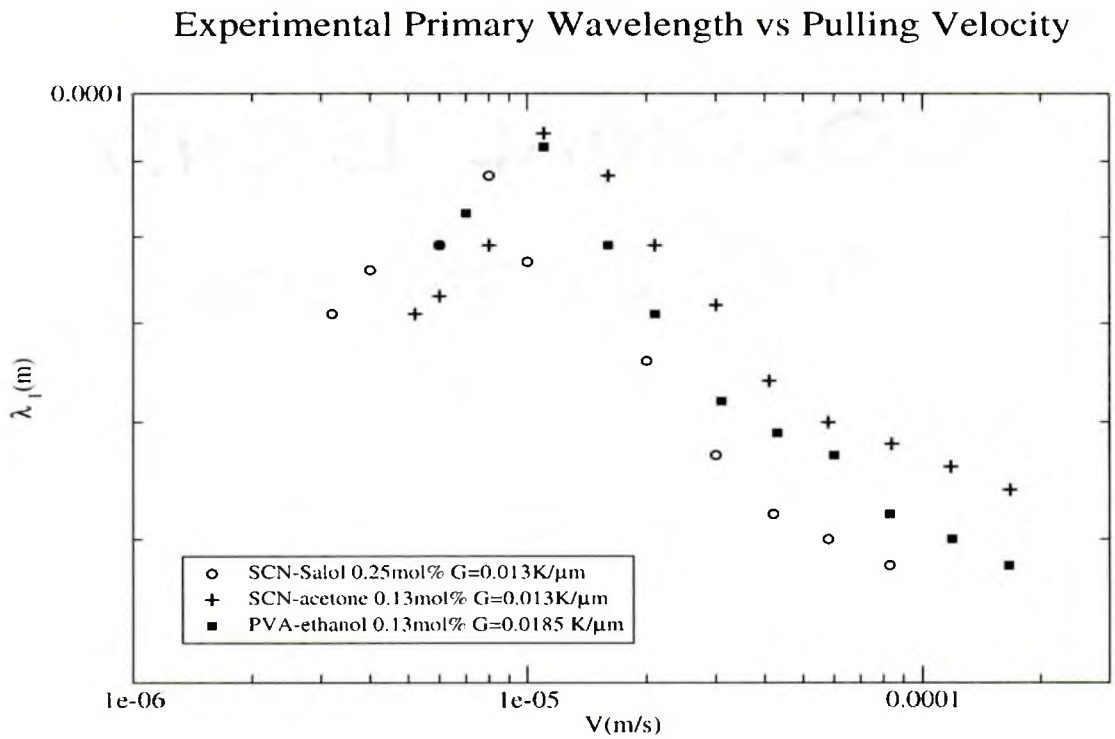

Figure 4.2: *Primary Wavelength(λ_1) vs Velocity(V) from experiments of PVA and SCN copied with permission from Refs[38, 42]*

The pivalic acid(PVA) experiments were run with 0.13mol% ethanol in a thermal gradient $G = 18.5K/mm$ and pulling velocities varied from $6\mu m/s$ to $166\mu m/s$. The PVA thermal capillary length $d_o^C = 1.11E-8m$, the liquid diffusion constant $D_L = 6E-10m^2/s$ and the partition coefficient $K = 0.16$.

The succinonitrile(SCN) experiments run with 0.13mol% acetone had a thermal gra-

dient $G = 13K/mm$ and pulling velocities varied from $5.2\mu m/s$ to $167\mu m/s$. The SCN thermal capillary length $d_o^C = 2.65E-8m$, the liquid diffusion constant $D_L = 9.2E-10m^2/s$ and the partition coefficient $K = 0.1$.

The succinonitrile(SCN) experiments run with 0.25mol% salol had a thermal gradient $G = 13K/mm$ and pulling velocities varied from $3.2\mu m/s$ to $83\mu m/s$. The SCN thermal capillary length $d_o^C = 2.65E-8m$, the liquid diffusion constant $D_L = 4E-10m^2/s$ and the partition coefficient $K = 0.2$.

The primary wavelengths(λ_1) were extracted from published plots of λ_1 vs V. This data is plotted in figure 4.2 and shows an increase in wavelength as the pulling velocity is increased above a critical value, a subsequent peak followed by a slower decrease in wavelength as the velocity continues to increase. We will use this data for comparison to our phase field simulations in Chapter 5.

4.2 Phase-Field Simulations

This section reports on our new directional solidification phase-field simulation data corresponding to 3 different alloys of PVA, cooled in 3 different gradients(1800K/mm, 625K/mm and 9.75K/mm) at various velocities ranging from the planar onset and into the dendritic regime. Figure 4.3 shows the growth of dendritic microstructures as a function of time in an alloy of PVA-0.813%ETH cooled at $V = 20\mu m/s$ and a gradient of $G = 9.75K/mm$.

One of the most fundamental issues confronting the investigation of dendritic microstruc-

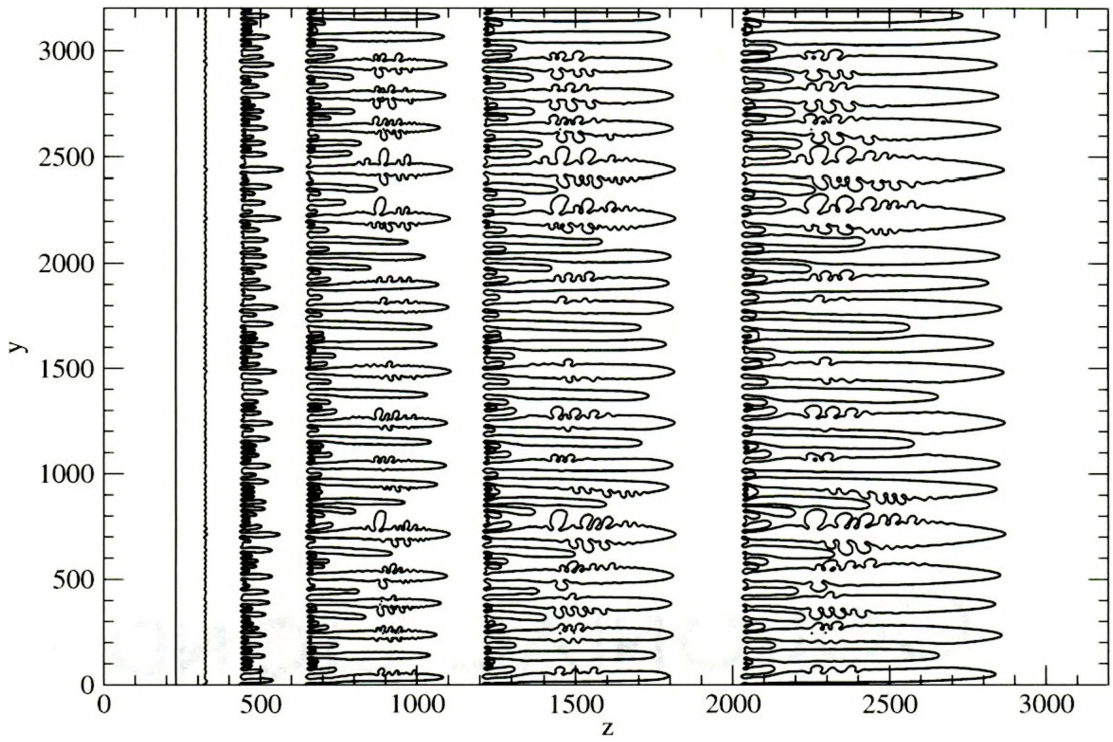

Figure 4.3: *The time evolution of the solid-liquid interface from a phase field simulation using parameters such that* $V = 20\mu m/s$ *and* $G = 9.75K/mm$ *at times of 4.8s, 13.5s, 16.4s,19.2s,23.1s and 29.8s*

ture selection is identifying the length scales characterizing the microstructure. In cases where solidification experiments are run for a very long time(such as the experiments discussed above[38, 42]) the identification of a primary wavelength is relatively straight forward. In more realistic situations, where the microstructure never quite reaches its ideal steady-state structure[3], the length scales that develop can be identified more precisely using a Power Spectral Analysis(PSA) technique(discussed in detail below). This method represents a relatively new approach to length scale measurements of this type[28]. The basic

[3]this is mainly the case for low cooling rates

idea of PSA is that it breaks up the power of a given signal into its component frequencies, indicating the relative importance of each frequency to the signal. In our implementation of PSA, the signal is the outline of the solid-liquid interface as shown in figure 4.3.

We ran numerous phase-field directional solidification simulations(such as in figure 4.3) and analyzed the time development of dendrite spacing using our PSA method. Our investigations revealed that in directional solidification the frequencies corresponding to the steady-state inter-dendritic spacings are established relatively early after the emergence of dendritic branches. Thus one of our main findings is the steady-state scale of primary interdendritic spacing sets in quite early, while less important scales(ie tip shape refinement) take much longer to establish. This will be discussed in more detail after we introduce in detail the PSA analysis methods.

4.2.1 Power Spectrum Analysis and Length Scale Extraction

PSA [21, 24, 72] uses the principles of fourier series to extract the various frequencies inherent in the data. Each frequency present in the data has a corresponding power connected to it which shows how strongly the data will exhibit that particular frequency. Spatial frequencies in data emerge when features are repeated periodically(such as dendrite fingers in directional solidification). As dendrites are the most obvious periodic feature in the data the power spectrum analysis is an ideal technique in which to characterize the structure.

Fourier's Theorem states *"a function f(x), having a spatial period L, can be synthe-*

sized by a sum of harmonic functions whose wavelengths are integral submultiples of L(L,$L/2$,$L/3$,$L/4$,etc.)"[21]. This can be represented mathematically by:

$$f(x) = \frac{A_o}{2} + \sum_m (A_m cos(2\pi \frac{m}{L} x)) + \sum_m (B_m sin(2\pi \frac{m}{L} x)) \tag{4.1}$$

where,

$$A_m = \frac{2}{L} \int_0^L f(x) cos(2\pi \frac{m}{L} x) dx \tag{4.2}$$

$$B_m = \frac{2}{L} \int_0^L f(x) sin(2\pi \frac{m}{L} x) dx \tag{4.3}$$

Fourier transformations can be applied onto any function f(x). However digital data does not have a continuous function f(x) defined at all points in space from 0 to L. Instead we have a discrete signal $f(n)$, $n = 1, 2..N$ where n is a discrete step corresponding to a distance Δx. The discrete fourier transform, an approximation of the continuous fourier transform, is given by

$$F_k = \sum_{n=0}^{N-1} (f(n) e^{-\frac{2\pi i n k}{N}}) \tag{4.4}$$

where the spatial frequency is given by $f_k = k/(N\Delta x)$, N is a data binning resolution defined such that $\Delta x = L/N$ and L is the system size.

This transformation, applied to the data for every frequency, will result in a corresponding complex function which upon taking the magnitude squared will result in a power spec-

trum $P_k = |F_k|^2$. Figure 4.4(bottom) shows a power spectrum of a directionally solidified dendritic array at a snapshot in time during solidification, figure 4.4(top). We clearly see a peak corresponding to a wavelength that closely matches the interdendritic spacing in the top figure. We note that this simulation was run to very late times so that the structures in figure 4.4 are close to steady state. We note secondary smaller peaks in the power spectrum, which correspond to the length scales such as the dendritic thickness, etc...

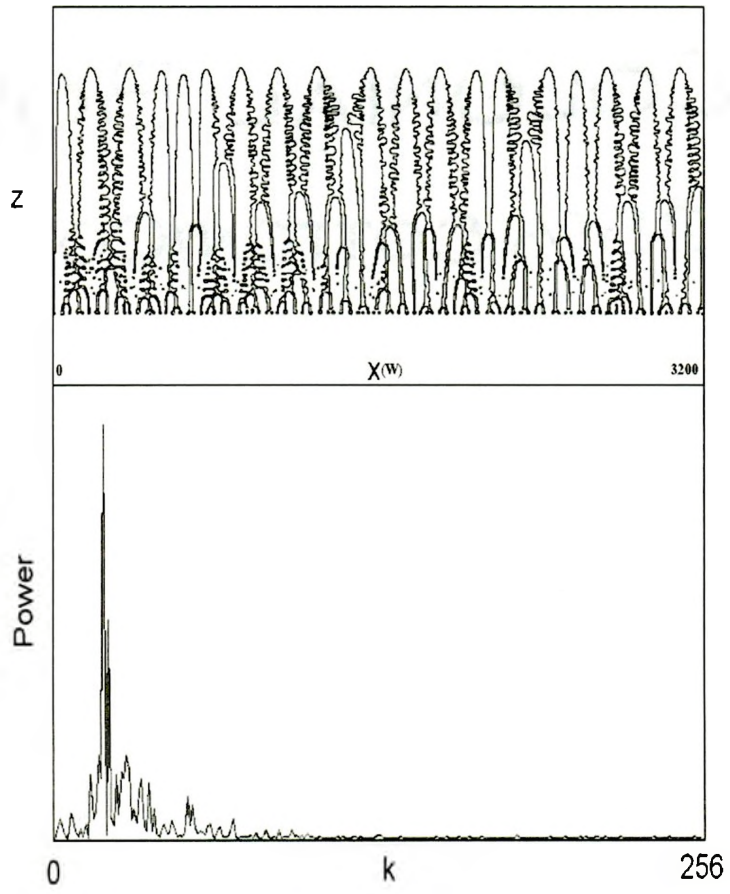

Figure 4.4: *Top: Interface position of dendritic array. Bottom: The corresponding power spectrum P_k vs $k = f_k L$.(The units W are defined in chapter 2 as the interface width.)*

4.2.2 Applying PSA to Dendritic Time Evolution

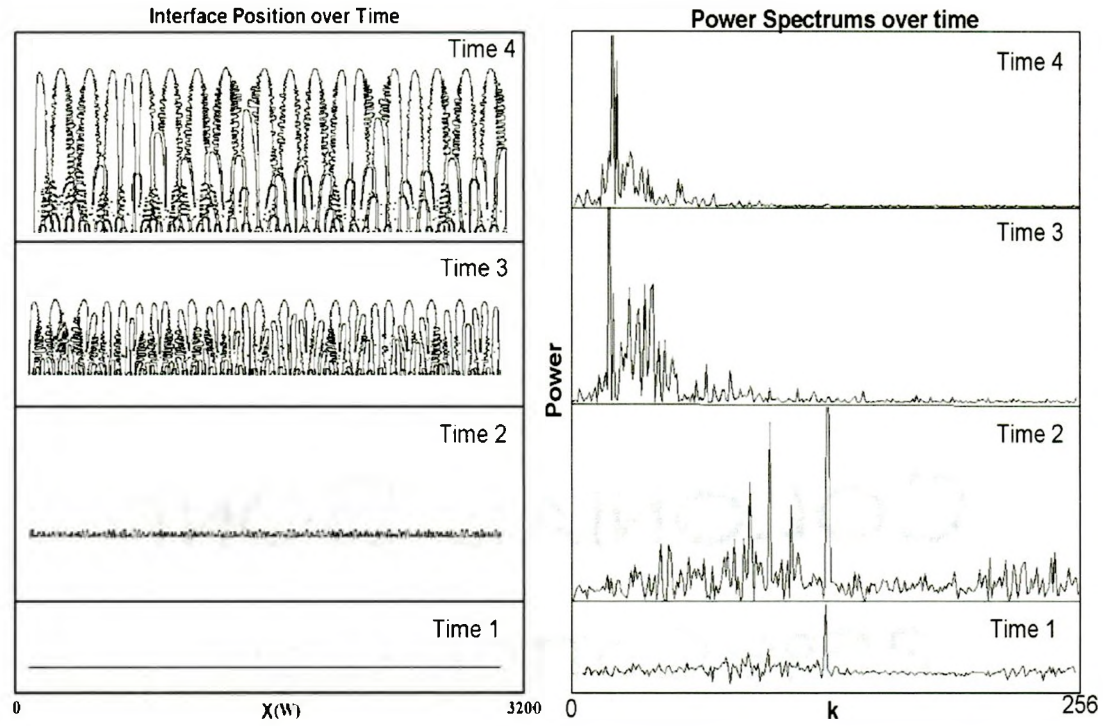

Figure 4.5: *(Right)The power spectrums of the evolution of interfacial growth. (Left) The corresponding interface profiles. Time1: Planar front begins to become unstable. Time2: The mullins-sekerka(MS) wavelength begins to emerge. Time3: The MS wavelength grows in amplitude, coarsens and selects a new wavelength. Time4: With late times the peak shifts in small amounts and the spread of k sharpens.*

Using our power spectrum analysis technique we can predict the time development of primary dendritic spacings. Figure 4.5 shows the power spectrum evolution over time and the corresponding dendritic structures for a PVA-0.813%ETH allow cooled at $V = 0.2$ and $G = 0.00191$, we find that as time progresses the peak shifts, but also the variance of the frequencies diminishes. Calculating the mean weighted average of the frequency over 256 frequencies,

$$k_{mean} = \frac{\sum_{k>0} k\, P_k}{\sum_{k>0} P_k} \equiv L/\lambda_1 \tag{4.5}$$

gives us the progression of the average primary dendrite spacing where L is the selection size and P_k is the corresponding power of frequency k/L.

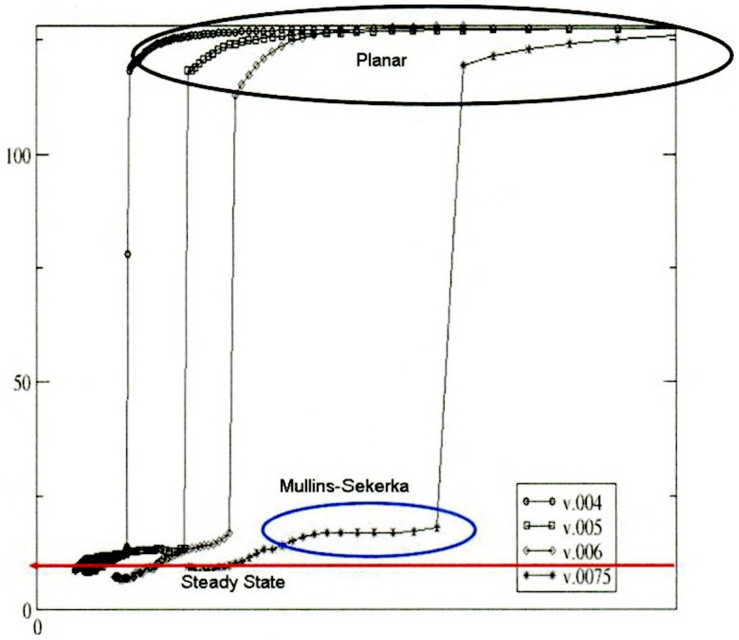

Figure 4.6: *k_{mean}, calculated from equation 4.5 plotted vs 1/time. Three distinct regions are shown, the planar interface, the MS wavelength and finally a steady state as $t \to \infty$.*

A plot of k_{mean} vs $1/time$ for 4 different pulling velocities is shown in figure 4.6 for the parameters shown in data set 1. There are 3 distinct regions of importance in this plot. The early time region is the planar front with random noise fluctuations, therefore the average is the expected k value of 128. When the interface breaks up new frequencies begin to grow and the Mullins-Sekerka instability emerges, the mean frequency plateaus for a time. Once the Mullins-Sekerka wavelengths grow to a finite amplitude dendrite fingers begin to

coarsen and the final steady state wavelength emerges. This wavelength can be extracted by interpolating the plots to the origin. Figure 4.7 shows a blow up of the $V = 0.006$ case from figure 4.6.

We simulated directional soldification in various alloys and used the above power spectrum analysis method to extract information about the time evolution and spacing selection of the steady-state inter-dendritic spacing. This data is discussed below.

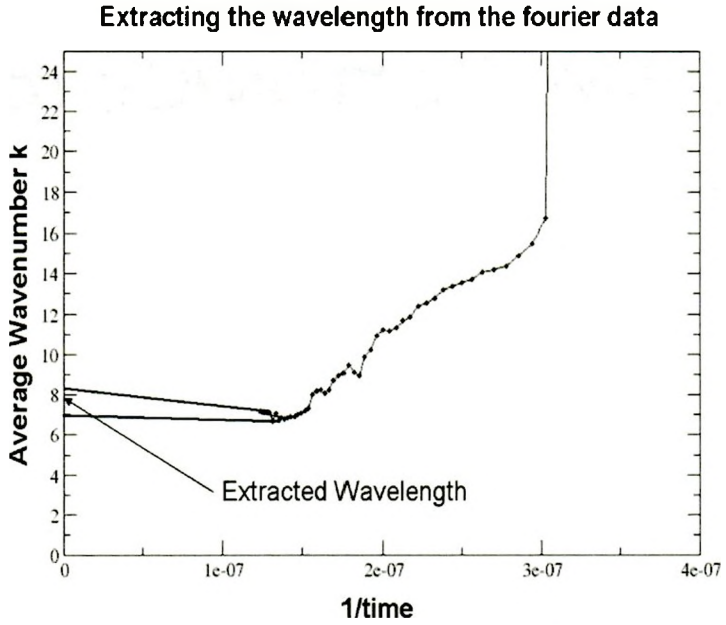

Figure 4.7: *For a single data run the steady state value can be extracted by interpolating* $1/time \to 0$. *The spread in the two solid lines indicates the bracket of error in extracting a steady-state wavenumber from our simulations. This error is about 1 wavenumber.*

4.2.3 Primary Wavelength Data

Data Set 1

Our first simulation modelled directional solidification in a PVA-10%ETH alloy cooled at various pulling velocities in a thermal gradient corresponding to 1800K/mm. The initial conditions were set such that the initial concentration profile in the liquid was in the steady state for a planar interface at the set pulling velocity of the interface. The velocity and the primary wavelength measurements, extracted using the power spectrum technique, are listed in table 4.1. Length was measured in units of $W = 3.12x10^{-8}m$ and time units of $\tau = 1.32x10^{-6}s$. Figure 4.8 (top) shows the concentration field for the data run where $V = 0.006$. Figure 4.8 (bottom) shows the interface position and the wavelength is extracted by applying the power spectrum technique to the data.

Velocity($\frac{W}{\tau}$)	**Wavelength** (W)		
0.004	200	**D**(W^2/τ)	0.8147
0.005	229	**K**	0.15
0.006	229	**G**(**K**/W)	0.002
0.0075	200	λ	1.3
0.01	178	C_o	0.1
0.03	123	$d_o^C(W)$	0.681

Table 4.1: Data Set 1

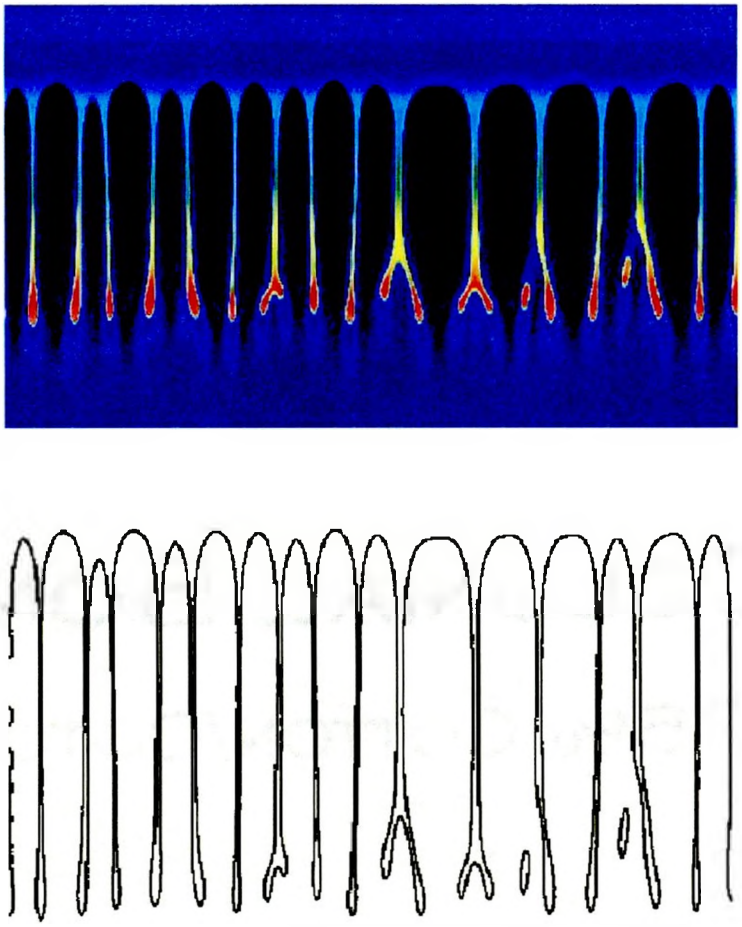

Figure 4.8: *Top: Concentration profile for* $V = 0.006$ *from data set 1. Red is high concentration black is low concentration. Bottom: The corresponding interface position is calculated by plotting the position of* $\phi = 0$

Data Set 2

Our second simulation modelled directional solidification in a PVA-10%ETH alloy cooled at various pulling velocities in a thermal gradient correstponding to 625K/mm. The initial concentration profile was set in both the solid and liquid as constant(no calculated profiles). The system was then allowed to naturally evolve and the concentration profile selected itself. The velocity and the primary wavelength measurements, extracted using the powerspectrum technique are listed in table 4.2. Length was measured in units of $W = 7.2x10^{-8}m$ and time units of $\tau = 1.62x10^{-5}s$. These runs see the first emergence of dendritic sidebranches. The interface and concentration data is plotted in figure 4.9 for $V = 0.07$.

Velocity($\frac{W}{\tau}$)	**Wavelength** (W)		
0.02	291	**D**(W^2/τ)	1.88
0.05	213	**K**	0.15
0.07	188	**G**(**K**/W)	0.0015
		λ	3
		C_o	0.1
		$d_o^C(W)$	0.295

Table 4.2: Data Set 2

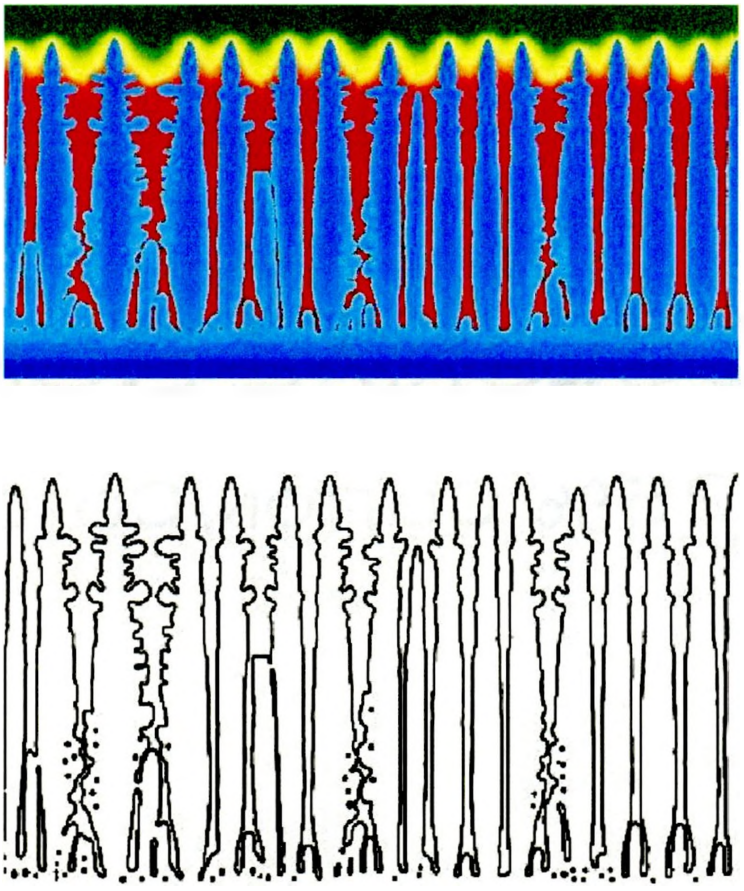

Figure 4.9: *Top: Concentration profile for* $V = 0.07$ *from data set 2. Red is high concentration blue is low concentration. Bottom: The corresponding interface position is calculated by finding* $\phi = 0$

Data Set 3

Our final simulation modelled directional solidification in a PVA-0.813%ETH alloy cooled at various pulling velocities in a thermal gradient correstponding to 9.7K/mm. This set is as in data set 2 where the initial concentration profile was set in both the solid and liquid to be constant. But we push the computational limit by increasing the parameter λ to 20. This allows us to run realistic gradients and system sizes and in a shorter amount of time we can run systems close to steady states in all regions of the primary wavelengths(The velocities are varied close to the planar onset and into the dendritic regime.) Length was measured in units of $W = 4.8x10^{-7}m$ and time units of $\tau = 4.81x10^{-3}s$. An example of this is shown in figure 4.10(both concentration fields and interfacial data).

Velocity($\frac{W}{\tau}$)	**Wavelength** (W)		
0.032	178	**D**(W^2/τ)	12.534
0.05	200	**K**	0.16
0.08	229	**G**(**K**/W)	0.00191
0.09	229	λ	20
0.1	200	C_o	0.00813
0.2	168	$d_o^C(W)$	0.0442
0.3	145		
0.6	114		

Table 4.3: Data Set 3

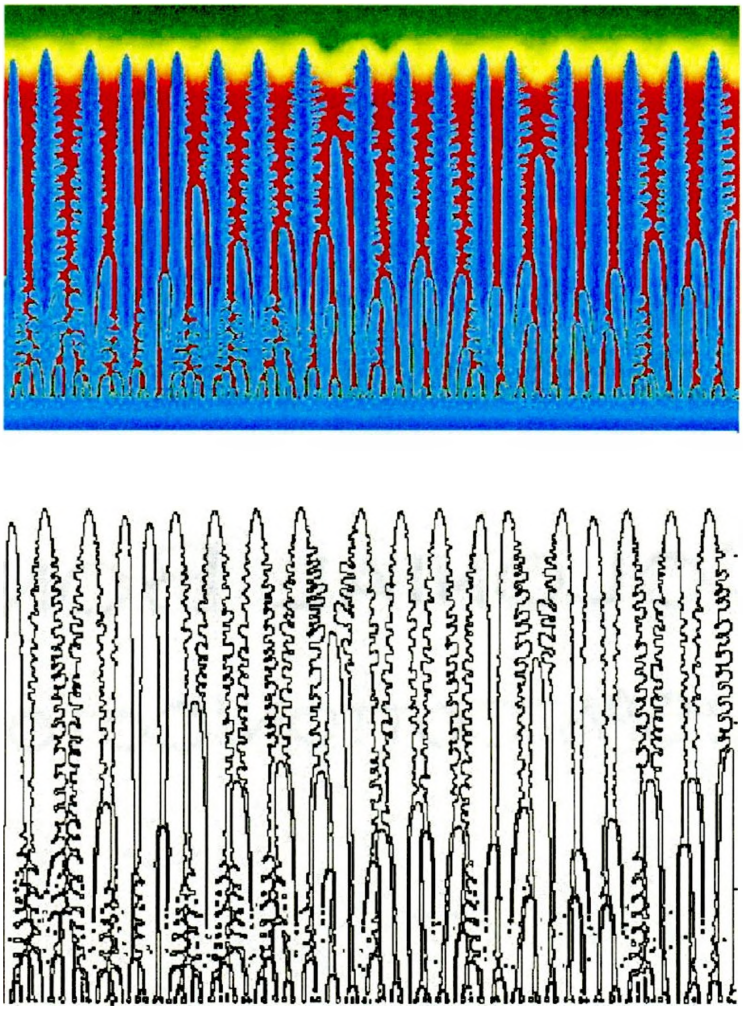

Figure 4.10: *Top: Concentration profile for* $V = 0.3$ *from data set 3. Red is high concentration blue is low concentration. Bottom: The corresponding interface position is calculated by finding* $\phi = 0$.

4.3 Primary Wavelength Selection

The primary wavelength λ_1 is plotted vs velocity in figure 4.11 for data set 1.

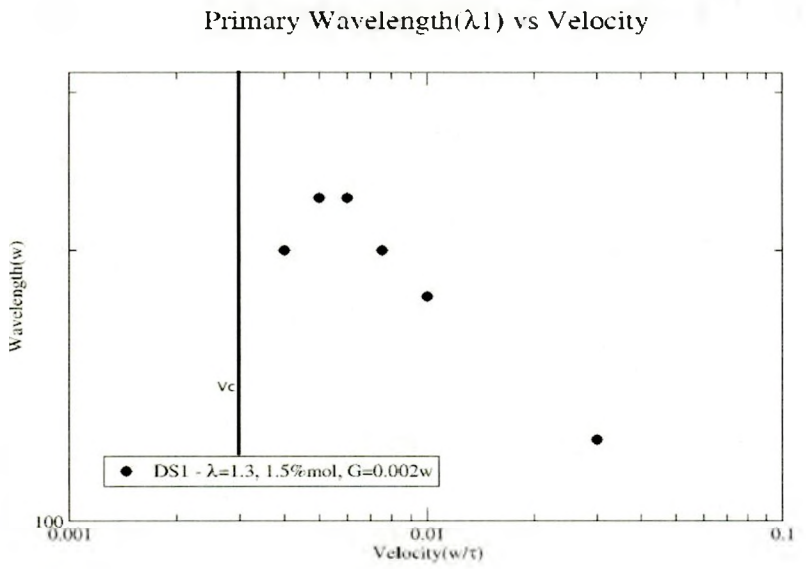

Figure 4.11: λ_1 *vs* V *for data set 1 in units of* ω *and* τ.

The solid vertical line is the boundary above which the mullins-sekerka planar instability develops, beyond this point the wavelength increases from a finite value, peaks and then decreases with increasing velocity. Figure 4.12 shows the primary wavelengths for all 3 of our simulated data sets. The inset shows the experimental data [42, 38, 31] of pivalic acid and succinonitrile from figure 4.2. In each case there is a critical planar velocity, an increase to a maximum, and a decreasing spacing as V is increased. Data set 2 does not feature a peak because we did not simulate any velocities small enough to produce the peak.

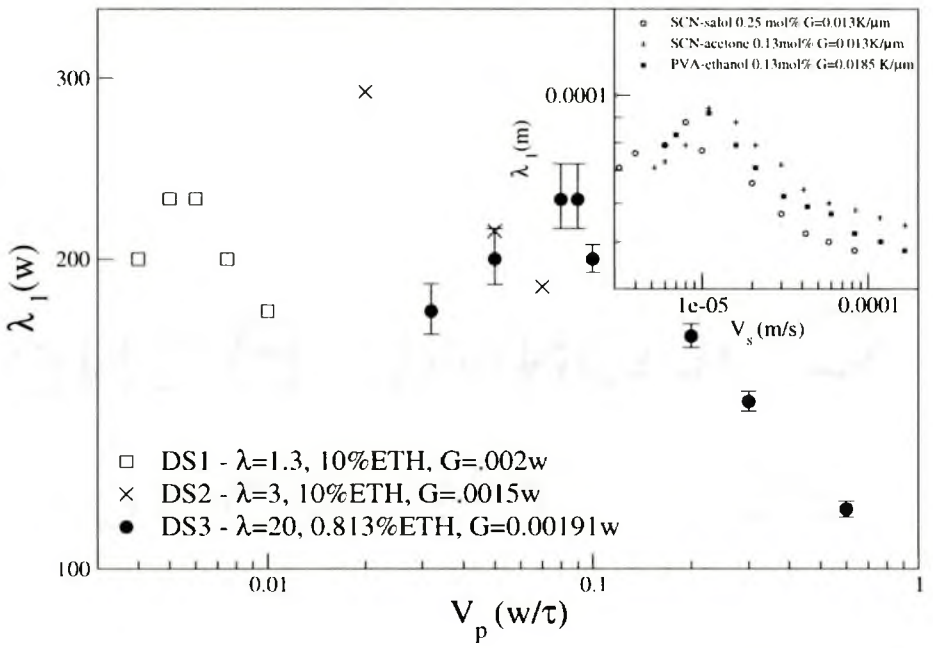

Figure 4.12: *All 3 data sets over plotted, errorbars are included for dataset 3 and errors are similar for the other two data sets. In the inset is experimental data from the literature[38, 42]. The difference in wavelengths between different alloy and processing parameters is evident.*

Figure 4.12 shows a clear dependence on λ_1 to both cooling rate (V and G) and alloy composition. We note that as a check of our power spectral method we initially collected data of the primary wavelengths of the dendrites in relation to their velocities by counting the peaks(figures 4.8-4.10) by hand for late times when the data coarsened and reached a steady state. The two approaches produce the same result.

Chapter 5

Scaling Primary Wavelengths

The data shown in chapter 4 shows a dependence of the inter-dendritic spacing as a function of the alloy concentrations and the solidification process parameters used. Previous research has involved the piecemeal fitting of regions of data to power laws[38, 69, 67] and the use of geometric arguments [39] in an attempt to predict primary wavelengths in directional solidification. Neither of these approaches produce one consistent theory that predicts the primary wavelengths over the entire range of cooling rates.

It was shown earlier in this thesis that the morphology of isolated dendritic crystals can be normalized to a single universal shape based upon the length scales of the crystal. Extending the notion of scaling to directionally solidified arrays of dendrites, we have created a new approach to wavelength prediction and have produced a unified scaling function that predicts primary wavelength in directional solidification as a function of the pulling velocity, thermal gradient and alloy composition. This chapter derives the properties of this

scaling formulation and describes the physical motivation behind it.

5.1 Scaling Theory

The premise of scaling is quite simple. A function is needed to map a given alloy's primary spacing λ_1 vs V curve to a universal curve featuring a dimensionless wavelength($\bar{\lambda}_1$) vs a dimensionless velocity($\bar{V}$). The universal curve is constructed by combining the length scales and reference points unique to each material. Returning to the plots of λ_1 vs V reported in chapter 4(figures 4.2 and 4.12), we can see some of the important features which will be key to this scaling analysis.

Each alloy exhibits a unique transition velocity(V_C) at which a planar front becomes unstable to the growth of cellular fingers. If a scaling function exists, then its origin(along the velocity axis) must coincide with this point. In chapter 1 a critical planar velocity is calculated using two methods. The first, and simpler, method is through constitutional supercooling but this method does not consider the capillarity effects of the interface in determining V_C. A more accurate calculation is through the second method, the mullins-sekerka linear stability analysis, which gives a modified V_C dependent upon capillarity.(Note: The accuracy of V_C becomes particularly important as $V \rightarrow V_C$ in the scaling curve.)

Next we examine figure 5.1 and note that with increasing velocity the planar interface becomes unstable, λ_1 increases, peaks and then decreases. The nature of this peak can be described by the competitive process of the diffusion length(l_D) and the thermal

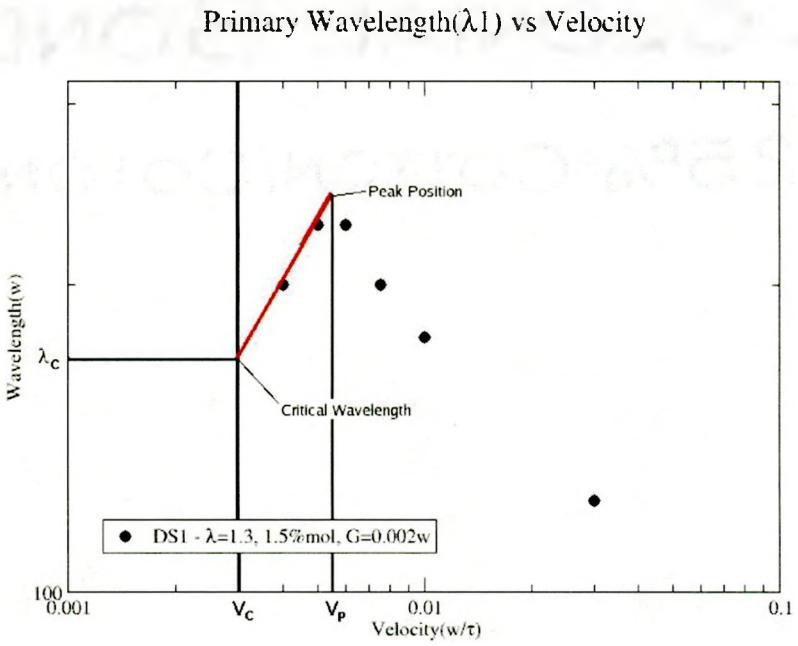

Figure 5.1: $\lambda_1 vs V$ *for dataset 1. Shown are* V_C, V_P *and the extrapolated* λ_C *all unique to this alloy and cooling parameters.*

length(l_T). As the velocity is increased the diffusion length decreases due to its velocity dependence(equation 1.14), while the traditional thermal length(equation 1.12) remains constant. Figure 5.2 plots the ratio of these two length scales at the extracted peak velocity for two of our simulated data sets and the three experimental data sets from Ref [42]. This ratio is found to be constant.

$$\frac{l_D}{l_T} \approx C \tag{5.1}$$

From equation 5.1 we can extract a theoretical velocity for the peak position as

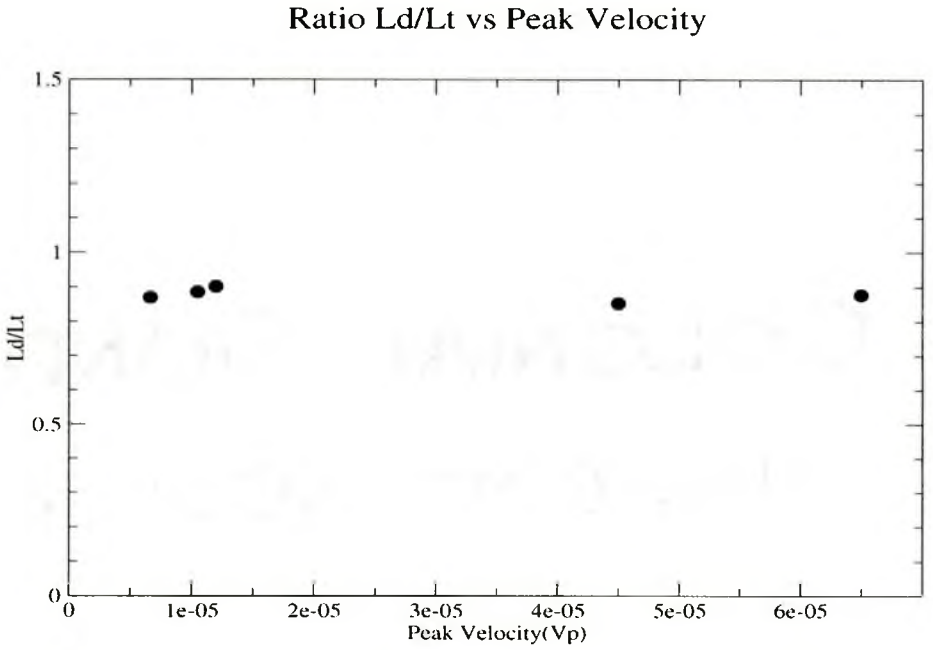

Figure 5.2: $\frac{L_D}{L_T}$ *as a funcion of the velocity of the peak* V_P*, the two points on the right were shifted by order of* 10^3 *to be shown on the plot.*

$$V_P = \frac{2D}{Cl_T} \tag{5.2}$$

Since V_P will play the role of a velocity scale we set $C = 1$.

Finally, extrapolating the upward branch of the raw $\lambda_1 vs V$ curves back to the velocity V_C(As in figure 5.1), it is clear that each alloy has its own unique onset steady state wavelength, denoted λ_C.(more will be said about obtaining this important length scale below)

Using the competitive process between l_D and l_T and the aforementioned points(V_C, V_P, λ_C), the axes of any given λ_1 vs V plot can be scaled such that all materials are mapped onto a single universal curve. This is done by scaling the velocity axis($\bar{V}$) to the critical and peak velocities as

$$\bar{V} = \frac{V - V_C}{V_p} \tag{5.3}$$

which can be more elegantly expressed in terms of the fundamental length scales as

$$\bar{V} = \frac{l_T}{l_D} - \frac{l_T}{l_D^*} \tag{5.4}$$

where l_D^* is the diffusion length at the critical velocity as calculated from mullin-sekerka instability theory(Chapter 1). Finally the wavelength($\bar{\lambda}_1$) axis is scaled to the onset wavelength λ_C, and multiplied by a ratio of the diffusion length to the thermal length. This gives,

$$\bar{\lambda}_1 = \frac{\lambda_1}{\lambda_C}\frac{l_D}{l_T} \tag{5.5}$$

After extracting λ_C for all our simulations as well as for all the data published in [38, 42] we can collapse all the data of figures 4.2 and 4.12(both experiments and phase field simulations) onto a single universal curve. This is plotted in figure 5.3

Applying the generality of the universal curve in figure 5.3 to all 2D directionally solidified alloys allows us to predict the inter-dendritic spacing of any(dilute) binary alloy.

Mathematically we can write the scaling function in figure 5.3[1] for the primary branch selection in the form

[1]Often referred to as a "crossover scaling function" since it captures the details of length scale selection continuously over different growth regimes.

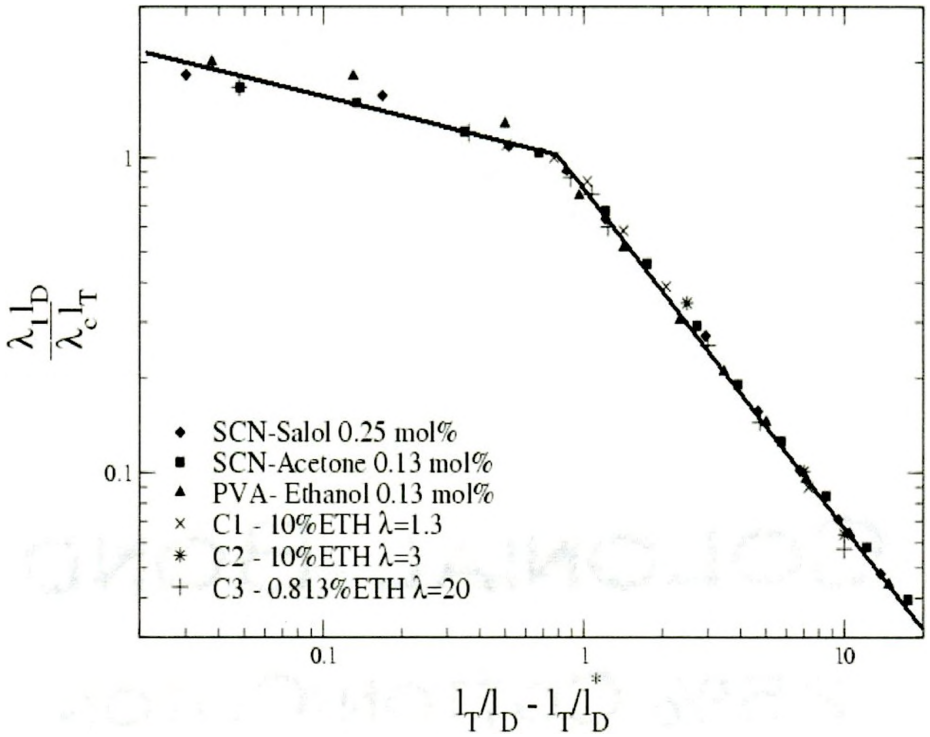

Figure 5.3: *The Computed and experimental data[38, 42] scaled to a single function using alloy and process length and velocity scales.*

$$\lambda_1 = \lambda_C \frac{l_T}{l_D} f(\frac{l_T}{l_D}) \tag{5.6}$$

where $f(\frac{l_T}{l_D})$ is the function plotted in figure 5.3(shifted by the material constant l_T/l_D^*.

This mapping shows that scaling works for different materials in the determination of the primary branches and it is remarkable in that it extends to the cellular regime on either side of the peak and, at higher velocities, into the dendritic regime. This scaling is dependent only on inherent length scales of a solidifying alloy and the onset critical wavelength. These length scales are easily calculated from the previous theoretical calculation shown in

this thesis, and $l_D^* = 2D/V_C$ where V_C is calculated from the mullins-sekerka analysis in Chaper 1. Let us turn now to the determination of λ_C.

5.2 Determination of λ_C

Because accurate data near V_C is difficult to obtain either numerically and experimentally, λ_C was selected so as to obtain the best data collapse to the universal curve of figure 5.3. Once λ_C was obtained we investigated its relation to the known length scales inherent in directional solidification. Two methods were used to theoretically calculate λ_C and are summarized below.

5.2.1 Tip Geometry

In this calculation we use the tip shape to geometrically determine λ_C as in [39]. We begin by finding λ_1 as in [39] which assumes that the tip shape can be approximated by an ellipsoid[2]. The ellipsoid has a tip radius R, a major axis a, and a minor axis b. The minor axis b is calculated from the following relation for ellipsoids

$$R \propto \frac{b^2}{a} \tag{5.7}$$

If we assume that the major axis is the amplitude of the tip(proportional to l_T), the

[2]While this method predicts the power laws of the primary spacing in the dendritic regime the wavelength is off from experimental values by a material dependent shift

tip radius is the mullins-sekerka wavelength λ_{MS}, while the steady state wavelength is the width of the ellipse($\lambda_1 = 2b$), as shown in figure 5.4, then the wavelength is extracted by solving equation 5.7 giving,

$$\lambda_1 = 2\sqrt{\lambda_{MS} l_T} \tag{5.8}$$

this predicts λ_C by calculating λ_{MS} at $V = V_C$

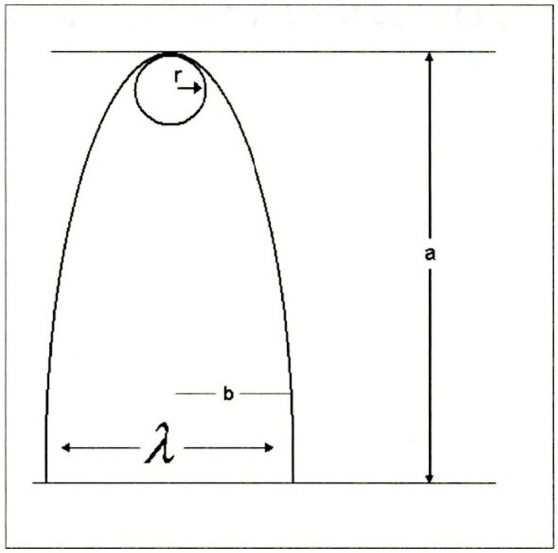

Figure 5.4: *Ellipsoidal tip shape, λ_1 is calculated by setting arrays of these and calculating the minor axis b*

Variable Thermal Length - l_{TR}

For large velocities the thermal length is constant. When $V \rightarrow V_C$ this is no longer true and the thermal length becomes a function of the velocity.

Figure 5.5 illustrates the steady-state concentration profiles of four different velocities

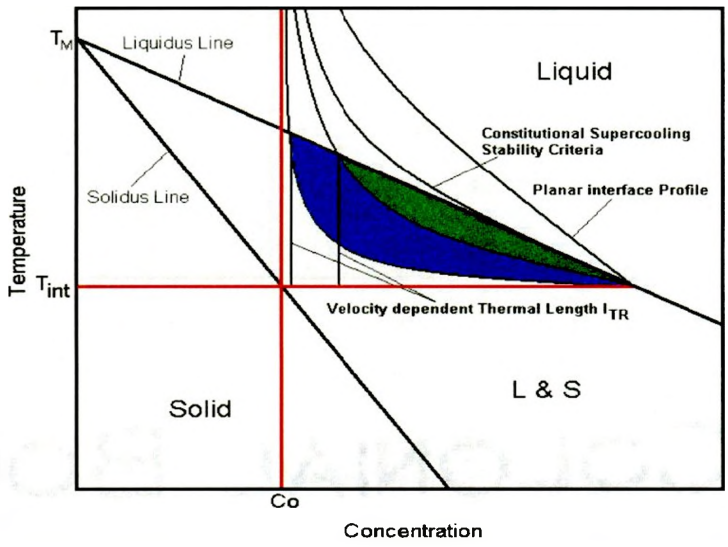

Figure 5.5: *Overlaying the concentration profile onto the binary phase diagram shows the conditions for a stable interface and illustrates the velocity dependent thermal length* $l_{TR}(V)$.

overlayed on a binary phase diagram with increasing velocity going from right to left. The lowest velocity represents the concentration profile ahead of the interface corresponding to a stable front. The next velocity consists of a profile that represents the critical velocity after which the interface will break up into cells or dendrites according to constitutional supercooling. The 4th velocity is the profile corresponding to the case where dendrite tips grow out to reach the maximum allowed amplitude l_T. The 3rd profile is the line of interest. This particular profile suggests that at some intermediate velocities(between planar solidification and maximum amplitude fingers reaching l_T) the amplitude of a primary dendrite tip is limited by the tip undercooling, which becomes dependent upon the velocity. [39, 29] We denote this amplitude scale $l_{TR}(V)$.

The calculation of l_{TR} starts similarly to the constitutional supercooling calculation.

We begin with equation 1.13 and from the phase diagram,

$$C_l = \frac{T_M - T}{m_l} \tag{5.9}$$

and the temperature in our directional solidification problem is given by

$$T = Gz + T_{int} \tag{5.10}$$

and from equation 5.9 we obtain $T_{int} = Tm - \frac{C_o}{K}m$. Equating both 5.9 and 1.13 results in a relation of the temperature, alloy composition, position, velocity and Diffusion as

$$\frac{T_M - T}{m_l} = C_o(1 + \frac{1-K}{K}e^{-\frac{z}{\frac{D}{v}}}) \tag{5.11}$$

By substituting equation 5.10 into equation 5.11 the crossover position on the phase diagram is calculated as

$$Gz = -C_o m_l(1 + \frac{1-K}{K}e^{-\frac{z}{\frac{D}{v}}}) + C_o\frac{m_l}{K} \tag{5.12}$$

Solving this equation for z explicitly is very difficult, but the equation can be further simplified in terms of existing length scales as

$$z = l_T(1 - e^{-\frac{z}{\frac{D}{v}}}) \tag{5.13}$$

solving equation 5.13 for z gives $z = l_{TR}(V)$

Calculating both the reduced thermal length(sets scale of the amplitude) and the mullins-sekerka wavelength(approximation of the tip radius) at the mullins-sekerka critical velocity V_C, we propose a revised prediction for λ_C as

$$\lambda_C = \sqrt{\lambda_{MS} l_{TR}(V_C)} \tag{5.14}$$

5.2.2 Alternate λ_C

An alternate form for λ_C is proposed in the literature[67, 42] and is taken by examination of the mathematical form of the Mullins-Sekerka wavelength. The Mullins-Sekerka wavelength can be approximated by $\lambda_{MS} \approx \sqrt{l_D d_o^C}$ for a planar interface in isothermal conditions. But the Mullins-Sekerka wavelength is calculated by assuming that the interface perturbation has a vanishingly small amplitude. By calculating l_{TR} at V_C and examining experimental amplitudes[38, 42] near V_C we note that the amplitudes are not vanishingly small. The addition of l_T is suggested in the literature to account for the non-zero amplitude in the form of the geometric mean of l_T, l_D and d_o^C

$$\lambda_C \propto (l_D d_o l_T)^{\frac{1}{3}} \tag{5.15}$$

5.2.3 Theory Comparison to Fit

The data in figure 5.3 was scaled to a selected λ_C so as to reach the best possible fit to the data. To test the viability of our prediction of λ_C(equation 5.14) as well as the prediction from the literature(equation 5.15) we show in figure 5.6 a plot of our extracted λ_C(the one leading to data collapse in figure 5.3) against the λ_C predicted in equations 5.14 and 5.15.

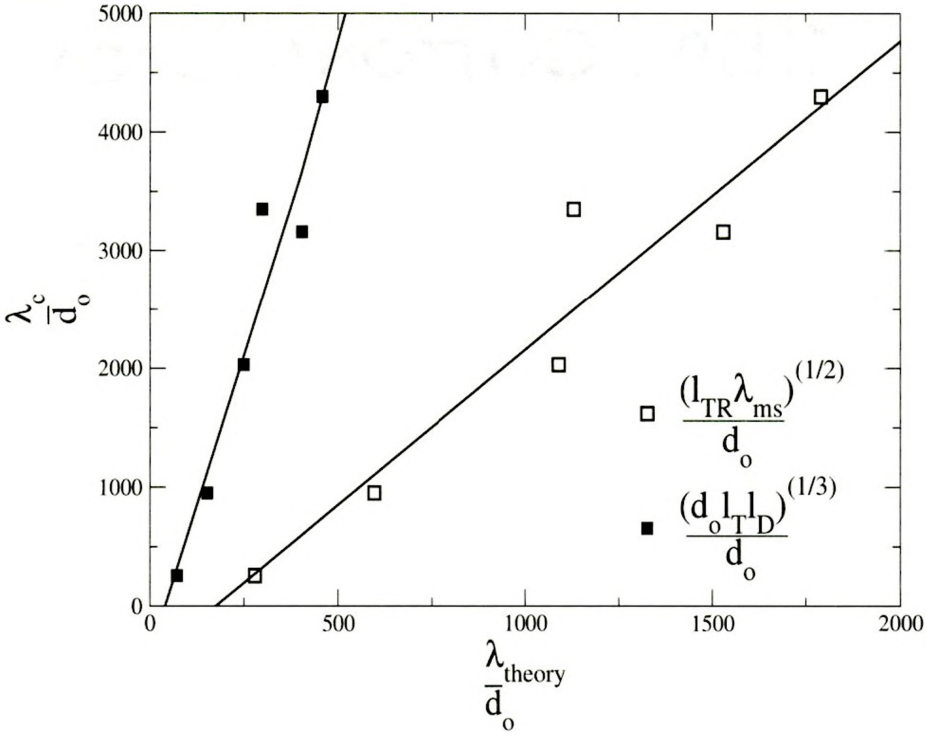

Figure 5.6: λ_C: *Fit plotted against two theoretical extractions in units of* d_o^C.

All values of λ_C were plotted in units of the capillary length d_o^C, to bring the data into a small enough range for better comparison. If either of the theories for λ_C from the literature were in agreement with our extracted λ_C from the experiments of [38, 42] and our phase

field simulations, we would expect

$$\lambda_C = \alpha \lambda_{theory} \tag{5.16}$$

While the relationship in figure 5.6 fits well to a linear function, the fit does not extrapolate through the origin and therefore we find an additional material dependent correction to the theoretical predictions of λ_C(equation 5.14 and 5.15). Specifically, our results(figure 5.6) predict instead

$$\lambda_C = \alpha \lambda_{theory}(1 + \frac{\beta d_o}{\lambda_{theory}}) \tag{5.17}$$

Inspection of equation 5.17 shows that $\lambda_C \propto \lambda_{theory}$ are in agreement only for large λ_C. This indicates that geometrical constructions of dendrite spacings that consider dendrite morphology as an ellipsoid are incorrect near the instability onset V_C.

Chapter 6

Conclusions

To summarize, we began, in chapter 1, with an overview of solidification, its applications and different methods in which it is studied. Pattern selection in solidification was characterized in terms of length scales. Directional solidification in particular was shown to be characterized by 3 lengths scales, the thermal length(l_T), the diffusion length(l_D) and the capillary length(d_o^C). We outlined the criteria for stability of a solidification front in the simple case of the constitutional supercooling limit and using the capillarity dependent Mullins-Sekerka instability analysis. From this analysis we could extract the initial instability wavelengths and calculate the planar to cellular onset velocity. Chapter 2 introduced the phase field method and overviewed a derivation of the phase field model for a binary alloy used in our work. Chapter 3 reviews numerical methods used to simulate the phase field model efficiently using adaptive mesh refinement methods. Chapter 4 reports on the data collected from our phase field simulations on primary wavelengths and which were

compared to published experimental data. The data was analyzed using a power spectrum algorithm applied to the solid/liquid interface. This technique was shown to be a robust way to analyze length scale selection in phenomena where multiple scales are competing.

The purpose of this thesis was to show that the length scale selection process in directional solidification was universal and that the interdendritic spacings could be predicted from material to material if the basic properties of the material and the process parameters were known. A scaling function was produced describing wavelength selection in directional solidification with the anisotropy parallel to the growth direction.

$$\lambda_1 = \lambda_C \frac{l_T}{l_D} f(\frac{l_T}{l_D}) \tag{6.1}$$

The data for three different experiments published in the literature and three experiments using phase field simulations were all shown to scale across a wide range of velocities, ranging from the low velocity regime of rising wavelength, into the cellular regime past the peak and also into the dendritic regime.(shown in figure 5.3) This scaling requires only knowledge of the three length scales(l_T, l_D and d_o^C) and the planar to onset velocity as calculated in chapter 1.

We have explicitly demonstrated scaling in 2D solidification, and would expect to find scaling collapse in 3D by repeating our analysis. Consequently, we would expect the selected wavelength in 3D to display a maximum for intermediate pulling velocities beyond V_C, similar to what was observed in the 2D case. We would also expect the scaling func-

tion to be very robust with respect to changes in the solid diffusivity and/or magnitude of surface tension anisotropy, as they simply renormalize V_C and λ_C. Future extensions of this work will involve an extension of our scaling analysis to spacing selection in strip-cast alloys.

Bibliography

[1] A.A.Wheeler, N.A.Ahmad, W.J.Boettinger, R.J.Braun, G.B.McFadden, and B.T.Murray. *Adv Space Res*, **16**:163, 1995.

[2] A.A.Wheeler, W.J.Boettinger, and G.B.McFadden. *Phys Rev A*, **45**:7424, 1992.

[3] A.Classen, C.Misbah, H.Muller-Krumbhaar, and Y.Saito. *Phys Rev A*, **43**:6920, 1991.

[4] A.Gonis, P.E.A.Turchi, and A.J.Ardell. *Materials Research Society Symposium Proceedings*, **580**:1, 1999.

[5] A.J.Simon, J.Bechhoefer, and A.Libchaber. *Phys Rev Lett*, **61**:2574, 1988.

[6] S. Akamatsu, G. Faivre, and T. Ihle. *Phys. Rev. E*, **51**:4751, 1995.

[7] Y.B. Altundas and G.Caginalp. *Jour. Stat. Phys*, **110**:1055, 2003.

[8] J. Bechhoefer and A. Libchaber. *Phys. Rev. B*, **35**:1393, 1987.

[9] E. Ben-Jacob, N. Goldenfeld, B.G. Kotliar, and J.S. Langer. *Phys. Rev. Lett.*, 53:2110, 1984.

[10] E. Ben-Jacob, N. Goldenfeld, J.S. Langer, and G. Schön. *Phys. Rev. Lett.*, 51:1930, 1983.

[11] W.J. Boettinger, J.A. Warren, C. Beckermann, and A. Karma. *Annu Rev. Mater. Res.*, **32**:163, 2002.

[12] M.H. Burden and J.D. Hunt. *J. of Crystal Growth*, 22:109, 1974.

[13] M.H. Burden and J.D. Hunt. *J. of Crystal Growth*, 22:99, 1974.

[14] B.Utter, R.Ragnarsson, and E.Bodenschatz. , 1999.

[15] G. Caginalp. *Arch. Rat. Mech. Anal.*, 92:205, 1986.

[16] G. Caginalp. *Phys. Rev. A*, 39:5887, 1989.

[17] G. Caginalp and W. Xie. *Phys. Rev. E*, 48:1897, 1993.

[18] S. R. Coriell, G. B. McFadden, and R. F. Sekerka. *Annu. Rev. Mater. Sci.*, **15**:119, 1985.

[19] D.A.Porter and K.E.Easterling. Phase transformations in metals and alloys 2nd ed. *Stanley Thornes Ltd*, 2001.

[20] E.Cadirli, N.Marasli, B.Bayender, and M.Gunduz. *Jour Mat Sci*, **34**:5533, 1999.

[21] E.Hecht. Optics 3rd ed. *Addison Wesley Longman*, 1998.

[22] K. R. Elder, Martin Grant, Nikolas Provatas, and Mike Kosterlitz. *Phys. Rev. E*, 64:1604, 2001.

[23] J.-M. Flesselles, A.J. Simon, and A.J. Libchaber. *Adv. in Phys.*, **40**:1, 1991.

[24] G.B.Arfken and H.J.Weber. Mathematical methods for physicists. *Harcourt/Academic Press*, 2001.

[25] B. Grossmann, K. Elder, M. Grant, and M. Kosterlitz. *Phys. Rev. Lett.*, 71:3323, 1993.

[26] J.J. Hoyt, M.Asta, and A.Karma. *Mat. Sci and Eng R*, R41-6, 2004.

[27] J.D. Hunt and K.A. Jackson. *Metall. Trans.*, **236**:843, 1966.

[28] D. Jasnow and J. Vinals. *Phys. Rev. A*, **41**:6910–6921, 1990.

[29] J.D.Weeks, W.Saarloos, and M.Grant. *Jour Crys Growth*, **112**:244, 1991.

[30] J.Jeong, N.Goldenfeld, and J.A.Dantzig. *Phys Rev E*, **64**:1063, 2001.

[31] J.S.Kirkaldy. *Met Trans A*, :1689, 1993.

[32] A. Karma. *Phys. Rev. Lett*, 87:115701, 2001.

[33] A. Karma and W.-J. Rappel. *Phys. Rev. E*, 53:3017, 1996.

[34] A. Karma and W.J. Rappel. *invited paper TMS*, , 1995.

[35] K.Brattkus and C.Misbah. *Phys Rev Lett*, **64**:1935, 1990.

[36] D. A. Kessler and H. Levine. *Phys. Rev. A.*, **31**:1712, 1985.

[37] D. A. Kessler and H. Levine. *Phys. Rev. A.*, **39**:3041, 1989.

[38] J. S. Kirkaldy, L. X. Liu, and A. Kroupa. *Acta Metall. Mater.*, **43**:2905, 1995.

[39] W. Kurz and D. J. Fisher. *Acta Metall.*, **29**:11, 1981.

[40] J.S. Langer. *Rev. Mod. Phys.*, 52:1, 1980.

[41] L. X. Liu and J. S. Kirkaldy. *Acta Metall. Mater.*, **28**:1029, 1993.

[42] L. X. Liu and J. S. Kirkaldy. *Acta Metall. Mater.*, **43**:2891, 1995.

[43] W. Losert, O. N. Mesquita, J.M.A. Figueiredo, and H.Z. Cummins. *Phys. Rev. Lett.*, **81**:409, 1998.

[44] W. Losert, B.Q. Shi, and H.Z. Cummins. *Proc. Natl. Acad. Sci. USA*, **95**:431, 1998.

[45] W. Losert, B.Q. Shi, and H.Z. Cummins. *Proc. Natl. Acad. Sci. USA*, **95**:439, 1998.

[46] H. Lowen, J Bechhoefer, and L.S.Tuckerman. *Phys Rev A*, **45**:2399, 1992.

[47] M.Conti. *Phys Rev E*, **55**:765, 1997.

[48] M.Conti. *Phys Rev E*, **60**:1913, 1999.

[49] M.E.Glicksman, M.B.Koss, and E.A.Winsa. *Phys Rev Lett*, 73:573, 1994.

[50] M.F.Ashby and D.R.H.Jones. Engineering materials: An introduction to their properties and applications. *Butterworth-Heinemann*, 1980.

[51] M.Glicksman. www.rpi.edu/locker/56/000756/index.html.

[52] W. W. Mullins and R. F. Sekerka. *J. Appl. Phys.*, **34**:323, 1963.

[53] P.E.Cladis, J.T.Gleeson, P.L.Finn, and H.R.Brand. *Phys Rev Lett*, **67**:3239, 1991.

[54] P.Kopczynski, W.Rappel, and A.Karma. *Phys Rev E*, **55**:1282, 1997.

[55] P.Oswald, J.Bechhoefer, and A.Libchaber. *Phys Rev Lett*, **58**:2318, 1987.

[56] N. Provatas and J. Dantzig. *The Enyclopedia of Materials Science and Technology*. World Scientific, Oxford, 2001.

[57] N. Provatas, J. Dantzig, and N. Goldenfeld. *Phys. Rev. Lett.*, 80:3308, 1998.

[58] N. Provatas, J. Dantzig, and N. Goldenfeld. *J. Comp. Phys.*, 148:265, 1999.

[59] N. Provatas, N. Goldenfeld, J. Dantzig, J.C. LaCombe, A. Lupulescu, M.B. Koss, M.E. Glicksman, and R. Almgren. *Phys. Rev. Let.*, **82**:4496, 1999.

[60] N. Provatas, Q. Wang, M. Haataja, and M. Grant. *Phys. Rev. Lett.*, 91, 2003.

[61] PZhao, M.Venere, J.C.Heinrich, and D.R.Poirier. *Jour Comp Phys*, **188**:434, 2003.

[62] R.D.Cook, D.D.Malkus, M.E.Plesha, and R.J.Witt. Concepts and applications of finite element analysis. *John Wiley and Sons inc*, 2002.

[63] R.J.Braun, G.B.McFadden, and S.R.Coriell. *Phys Rev E*, **49**:4336, 1994.

[64] R.Trivedi and K.Somboonsuk. *Mats Sci and Eng*, **65**:65, 1984.

[65] M. Sabouri-Ghomi, N. Provatas, and M. Grant. *Phys Rev Lett*, **86**:5084, 2001.

[66] A. Schmidt. *J. Comp. Phys.*, 125:293, 1996.

[67] R. Trivedi and W. Kurz. *Acta metall. mater.*, **42**:15, 1994.

[68] R. Trivedi, Shan Liu, B. Echebarria, and A. Karma. *TMS*, 2004.

[69] R. Trivedi and K. Somboonsuk. *Mat. Sci. and Eng.*, **65**:65, 1983.

[70] B. Utter, R. Ragnarsson, and E. Bodenschatz. *Phys. Rev. Lett.*, **86**:4604, 2001.

[71] W.D.Calister. Materials science and engineering an introduction. *John Wiley and Sons inc*, 2003.

[72] W.H.Press, S.A.Teukolsky, W.T.Vetterling, and B.P.Flannery. Numerical recipes in c. *Cambridge University Press*, 1992.

[73] X.Tong, C.Beckermann, A.Karma, and Q.Li. *Phys Rev E*, **63**:1063, 2001.

[74] Y.Kim, N.Provatas, N.Goldenfeld, and J.Dantzig. *Phys Rev E*, **59**:2546, 1999.

[75] Y.Lu, C.Beckermann, and A.Karma. *Proceedings of IMECE2002*, , 2002.